



CHALMERS
UNIVERSITY OF TECHNOLOGY

Semiconductor-based electron flying qubits: review on recent progress accelerated by numerical modelling

Downloaded from: <https://research.chalmers.se>, 2024-04-19 01:35 UTC












Citation for the original published paper (version of record):

Edlbauer, H., Wang, J., Crozes, T. et al (2022). Semiconductor-based electron flying qubits: review on recent progress accelerated by numerical modelling. EPJ Quantum Technology, 9(1). <http://dx.doi.org/10.1140/epjqt/s40507-022-00139-w>

N.B. When citing this work, cite the original published paper.



Semiconductor-based electron flying qubits: review on recent progress accelerated by numerical modelling

Hermann Edlbauer¹ , Junliang Wang¹ , Thierry Crozes¹, Pierre Perrier¹, Seddik Ouacel¹, Clément Geffroy¹, Giorgos Georgiou^{1,2,3}, Eleni Chatzikyriakou² , Antonio Lacerda-Santos², Xavier Waintal² , D. Christian Glatthil⁴ , Preden Roulleau⁴ , Jayshankar Nath⁴, Masaya Kataoka⁵ , Janine Splettstoesser⁶ , Matteo Acciai⁶ , Maria Cecilia da Silva Figueira⁷, Kemal Öztas⁷, Alex Trellakis⁷, Thomas Grange⁸, Oleg M. Yevtushenko⁷ , Stefan Birner^{7*} and Christopher Bäuerle^{1*} 

*Correspondence:
stefan.birner@nextnano.com;
christopher.bauerle@neel.cnrs.fr

⁷nextnano GmbH,
Konrad-Zuse-Platz 8, 81829
München, Germany

¹Univ. Grenoble Alpes, CNRS,
Grenoble INP, Institut Néel, 25 rue
des Martyrs, 38000 Grenoble, France
Full list of author information is
available at the end of the article

Abstract

The progress of charge manipulation in semiconductor-based nanoscale devices opened up a novel route to realise a flying qubit with a single electron. In the present review, we introduce the concept of these electron flying qubits, discuss their most promising realisations and show how numerical simulations are applicable to accelerate experimental development cycles. Addressing the technological challenges of flying qubits that are currently faced by academia and quantum enterprises, we underline the relevance of interdisciplinary cooperation to move emerging quantum industry forward. The review consists of two main sections:

Pathways towards the electron flying qubit: We address three routes of single-electron transport in GaAs-based devices focusing on surface acoustic waves, hot-electron emission from quantum dot pumps and Levitons. For each approach, we discuss latest experimental results and point out how numerical simulations facilitate engineering the electron flying qubit.

Numerical modelling of quantum devices: We review the full stack of numerical simulations needed for fabrication of the flying qubits. Choosing appropriate models, examples of basic quantum mechanical simulations are explained in detail. We discuss applications of open-source (KWANT) and the commercial (nextnano) platforms for modelling the flying qubits. The discussion points out the large relevance of software tools to design quantum devices tailored for efficient operation.

Keywords: Quantum computers; Electron flying qubits; GaAs/AlGaAs based nanodevices; Modelling quantum nanodevices

1 Introduction

Flying qubits are originally intended to serve as a communication link within a quantum computer [1] and represent a vital part of global road-maps towards secure data transmission – the so-called quantum internet [2]. Recently, in-flight manipulations of photon-

© The Author(s) 2022. This article is licensed under a Creative Commons Attribution 4.0 International License, which permits use, sharing, adaptation, distribution and reproduction in any medium or format, as long as you give appropriate credit to the original author(s) and the source, provide a link to the Creative Commons licence, and indicate if changes were made. The images or other third party material in this article are included in the article's Creative Commons licence, unless indicated otherwise in a credit line to the material. If material is not included in the article's Creative Commons licence and your intended use is not permitted by statutory regulation or exceeds the permitted use, you will need to obtain permission directly from the copyright holder. To view a copy of this licence, visit <http://creativecommons.org/licenses/by/4.0/>.

number states (so-called Fock states) have shown that the flying qubit architecture can also be applied as a stand-alone quantum processing unit [3]. Owing to this progress on photonic quantum-computation approaches [4, 5], flying qubits are typically associated with photons [6]. Employing so-called “time multiplexing” architectures, photonic quantum computing can in principle scale up to millions of qubits. The strongly probabilistic nature of photonic two-qubit gates renders the far-reaching photonic coherence however a double-edged sword making the realisation of photonic quantum computing challenging. Though, a flying-qubit architecture can also be built on the basis of other quantum systems such as the electron [7]. The charge of an electron causes Coulomb interaction with its electro-magnetic environment, which exposes its quantum properties to decoherence but enables well-controlled single-particle manipulations and multi-qubit coupling.

Historically, flying qubits stem from the research field of quantum optics which addresses – in opposition to wave optics – the granular nature of light. The need to control the ultimate grain of light – a single photon – led to the advent of the first single-photon source in 1974 [8] and over several decades, various promising approaches have been developed [9]. A prominent example are deterministic single-photon sources based on quantum dots (QD) [10, 11]. Since these photon emitters allow for efficient coupling to a nanophotonic cavity [12, 13] and provide a high degree of indistinguishability [14, 15] and brightness [16–18], they turned out as highly suitable sources for quantum communication [6]. Yet, the extraction efficiencies of quantum dot based single-photon sources are not at the level to perform photonic quantum computing. Nevertheless, the demand for photonic components such as on-demand single-photon sources, quantum photonic processors and single-photon detectors fostered the emergence of start-ups such as *Quandela*,¹ *QuiX*,² or *SingleQuantum*,³ to name a few. Photonic quantum computing is currently pursued by the start-up *PsiQuantum*⁴ which uses heralded photons. Here parametric down conversion is used to create from a non-deterministic single photon source a pair of photons serving as signal and idler. Measuring the idler photon with an additional single-photon detector ensures that indeed a single photon (signal) has been generated – however, at the expense of additional hardware.

In order to implement photonic quantum computation, two-qubit gates are a necessity. As photons do not interact, operating two-qubit gates on physical qubits is very difficult. It is possible in theory to use non-linear effects such as Kerr effects, but these effects are so small that it is not possible in practice, at least in known media [5]. Another route is to use photon detectors and the associated projective measurement as a way to entangle photons. While photon detectors can indeed produce entanglement they do so in a probabilistic way, i.e. depending on the result of the measurement, the remaining state will be entangled or not. However, such probabilistic gates cannot be used on a large quantum computer as the probability for the correct circuit to be applied will decay exponentially with the number of two-qubit gates. Protocols have been proposed (such as the Knill–Laflamme–Milburn protocol) [4] trying to mitigate this issue and to enhance the probability for the correct gate to be applied. This approach comes however along with significant cost since many ($n \gg 1$) ancilla photonic qubits are required to guarantee that

¹<https://quandela.com>

²<https://www.quix.nl>

³<https://singlequantum.com>

⁴<https://psiquantum.com>

the correct gate is applied (with an error probability of the order of $1/n$) [5]. From this point of view, the development of non-photonic approaches represents a promising and competitive avenue.

For sake of completeness, let us also point out a different approach to photonic quantum computing based on so-called *squeezed states*. Here the qubits are generated as a superposition of multiple photons in a light pulse. This approach is pursued by the start-up *Xanadu*.⁵ It has conceptual similarity to the Leviton single-electron transport which will be presented below in Sect. 2.3.

As for photons, electron quantum optics started by probing the discrete nature of the electrons. The granularity of electrons was undermined by the quantum fluctuations of the current [19] – the so-called shot noise – similar to photon noise [20, 21]. The first experiments mimicking textbook experiments of quantum optics, but with electrons, date back to 1999 with electronic Hanbury Brown and Twiss experiments [22–24]. These achievements were succeeded by the realisation of the first electronic Mach–Zehnder interferometer [25], a quantum device that nicely shows up the wave nature of the electron and which is a key tool for qubit manipulation. All of these pioneering experiments that fostered the idea of electronic quantum control for computing applications have however been performed applying a DC current – meaning a continuous stream of billions of electrons. Only in 2007 the invention of the first single-electron sources [26] opened up the possibility of performing electron-quantum-optics experiments at the single-particle level. This achievement triggered tremendous progress on electron quantum optics over the last two decades bringing various single-electron sources [26–30] that reach now emission efficiencies larger than 99% [30–34] – a value far superior to latest single-photon sources [11, 16, 18, 35, 36]. Besides emission, also single-electron detection has significantly progressed. Whenever a single electron is captured on a sufficiently long timescale – of the order of a microsecond or more – also detection efficiencies well above 99% are achieved [31, 32]. The efficient control on the single-particle level points out the large potential to exploit single flying electrons for quantum applications.

From measurements on charge qubits in stationary double quantum dots [37–40], the coherence time of electron flying qubits is expected to be of the order of a few nanoseconds. Decoherence is, thus, the major obstacle for quantum implementations with single flying electrons. The young research field of electron quantum optics is however constantly producing new findings bringing the coherence properties of flying electrons closer to macroscopic scales [41–44]. From the quantum-computation perspective, the central figure of merit is the number of operations that can be performed within the coherence time. At present, this number is about 1000 for leading approaches such as superconducting qubits, trapped ions, or spin qubits [45–49]. In order to achieve such operation fidelity with electron flying qubits, a time control at the picosecond scale is required. Such ultrafast in-flight manipulation is presently being pursued in the FET-Open project *UltraFastNano* [50].

The EU project *UltraFastNano*⁶ aims to advance ultrafast operations in nanoelectronic devices to demonstrate the first electron flying qubit. The concept is similar to that of a photonic quantum computer but, instead of photons, electrons are used as carrier of

⁵<https://www.xanadu.ai>

⁶www.ultrafastnano.eu – <https://cordis.europa.eu/project/id/862683>

quantum information. The project is a concrete example where the academic and the industrial sector are joining forces to develop and benchmark the tools that are required by the value chain of emerging quantum industry. Often, the initial market of tools for sufficiently advanced technologies is too small to be pursued by larger corporations, opening a niche-market opportunity for small and medium-sized enterprises (SME). This demand is satisfied by the industrial partner *nextnano GmbH*⁷ – an SME based in Munich (Germany) with 12 employees and 300 customers in more than 35 countries – which develops a software tool calculating the quantum mechanical properties of semiconductor nanodevices. The synergy of academic and industrial partners on numeric simulations and experimental implementations within *UltraFastNano* fosters progress on electron flying qubits opening a novel branch of quantum industry.

In this article, we review three promising experimental routes towards electron-flying-qubit implementations and discuss the potential of numerical simulations to speed up experimental development cycles towards quantum-computing applications. The reviewed experimental pathways differ mainly in the way the electron qubit is transported. In particular, we address single-electron transport by means of a surface-acoustic wave, emission from a quantum-dot pump and Levitons. For each transport approach, we point out the specific aspects where numerical simulations are key to unveil efficient routes for follow-up implementations. Identifying these target aspects of cutting-edge electron-quantum-optics experiments, we finally present generic numerical simulations providing insights that are decisive for the development stages towards electron flying qubits. Confronting numerical simulations with latest experimental results, we point out the capability of the numerical simulations to guide experimental implementations faster to success.

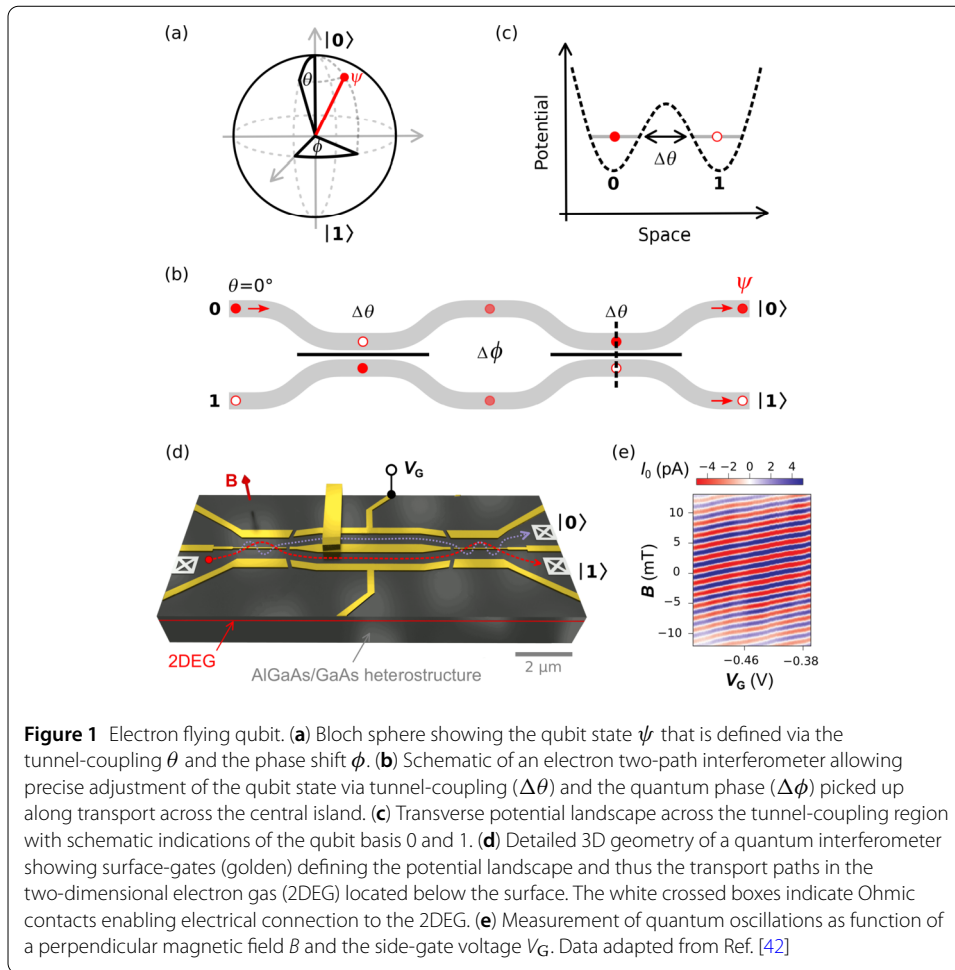
2 Pathways towards the electron flying qubit

Different than for a classical bit where the states 0 and 1 basically correspond to the charging state of a capacitor, the electron flying qubit is defined via the presence of a single electron in two paths of transportation. The quantum state of the thus-defined flying qubit can be depicted on a Bloch sphere as shown in Fig. 1a. The north and south pole of the sphere represent the classical states of the electron being in one of the two paths of transportation (0 and 1). The probability to end up in one of these states is represented via angular coordinates of the sphere θ and ϕ that make up the quantum state ψ :

$$|\psi\rangle \propto \cos\left(\frac{\theta}{2}\right)|0\rangle + \sin\left(\frac{\theta}{2}\right) \cdot \exp(i\phi)|1\rangle. \quad (1)$$

The thus-defined quantum state of the flying electron is fully controllable in an electronic Mach–Zehnder interferometry setup as sketched in Fig. 1b. The quantum interferometer hosts two regions where the paths of transportation approach each other and couple via a narrow potential barrier (see horizontal lines). According to the potential landscape within this coupling region – see Fig. 1c –, the flying qubit state undergoes periodic oscillations (angle θ) caused by coherent tunneling. In between the two tunnel-coupled regions, the flying qubit picks-up a quantum phase ϕ that is tunable via the potential along the two paths and the enclosed magnetic flux. Employing a surface-gate-defined quantum

⁷ www.nextnano.com



interferometer realised in a GaAs-based heterostructure (see Fig. 1d), basic quantum operations of such an electronic flying qubit have already been successfully demonstrated (see Fig. 1e) with a continuous current of electrons [42]. The big challenge ahead is to perform such quantum state control on the level of single electrons and to couple several of the so-obtained electron flying qubits to generate a set of non-local entangled quantum states.

In semiconductor devices, a single electron is manipulable in a surface-gate-defined nanoscale structure such as a quantum dot or a waveguide. The majority of such implementations are performed within the two-dimensional electron gas (2DEG) formed near the surface of a GaAs-based heterostructure [7], which have typically coherence lengths of several tens of micrometers [41, 42, 51, 52]. Applying a set of negative voltages on these gates, one can shape the potential landscape in the 2DEG and thus form and control the nanoscale devices. So far, there are two methods to guide the electrons along the desired paths: electrostatic waveguides [42, 53] or – at high magnetic field – quantum-Hall edge states [25, 54]. The 2DEG quality has been continuously improved [55, 56] and combined with clever device design [41], which allowed to push the phase coherence length up to several hundreds of micrometers in recent experiments [43].

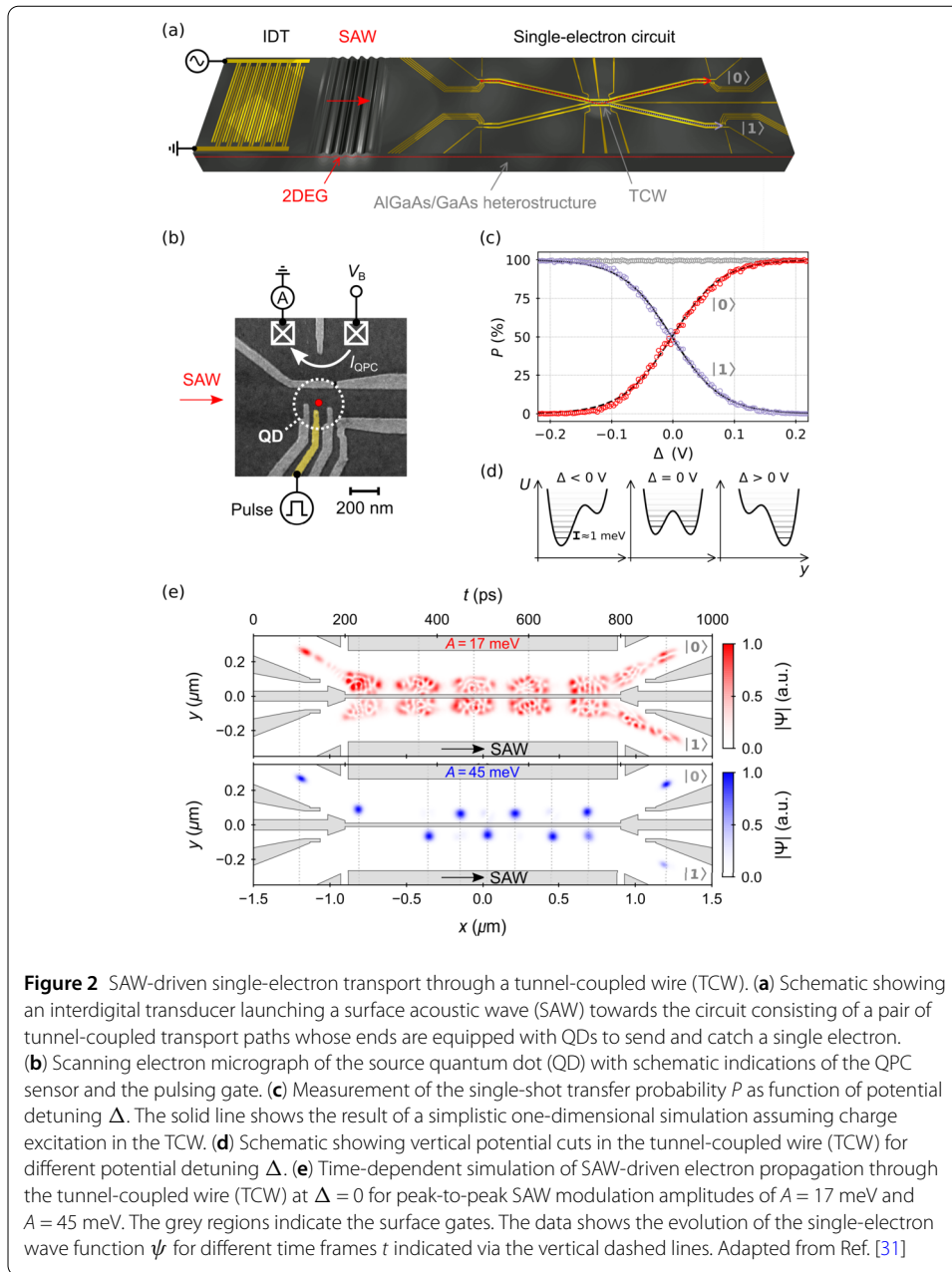
The availability of quantum dots serving as highly efficient single-electron sources and receivers led to the development of single-electron-transport techniques based on sur-

face acoustic waves [28, 29, 57] and voltage-modulation pumping [58, 59]. Fostered by technological progress and a growing understanding of the underlying physical mechanisms [60], these approaches now achieve transfer efficiencies well above 99% [31–34]. The quantum-dot-based transport systems represent the electronic counterpart to the deterministic single-photon source we have mentioned earlier. Besides that, different avenues have been explored such as the so-called Leviton that is a well-protected collective single-electron excitation generated by an ultrafast Lorentzian voltage pulse [30, 61, 62]. As the aforementioned photonic squeezed state that is a special kind of a coherent laser pulse, a Leviton represents a special form of a classical voltage pulse. The progress in these experimental routes – surface acoustic waves, electron pumps and Levitons – opened up the way to realise a flying-qubit platform with electrons instead of photons. In the following sections, we outline these three conceptually different approaches towards the electron flying qubit in more detail and discuss how numerical simulations have played a key role to interpret the experimental results guiding nanodevice design to the next generation.

2.1 Electron qubits surfing on a sound wave

In III-V semiconductor compounds, such as the presently discussed GaAs-based devices, sound is accompanied by an electric potential wave due to its piezoelectric properties allowing charge displacement [63]. At the first glance, acousto-electric transport seems a rather brute approach to move an electron qubit. A surface acoustic wave (SAW) has proven itself however as an efficient and well-controllable transport medium. Figure 2a shows a schematic of the single-electron transport approach. A SAW is typically generated with an interdigital transducer (IDT) – a device that is well established in modern consumer electronics products [64]. Applying a finite, resonant input signal on the IDT, a SAW is emitted which then travels relatively slowly with a characteristic speed of about $3 \mu\text{m ns}^{-1}$ towards a surface-gate-defined nanoscale device [65]. The circuit is constructed on the basis of fully depleted transport channels whose ends are equipped with QDs – see Fig. 2b – serving as highly efficient single-electron source and receiver. Each QD is equipped with an adjacent quantum point contact (QPC) allowing to trace its charge occupation. After loading a single electron at the source QD via a sequence of voltage variations on the corresponding surface gates, a SAW is emitted. The SAW train typically has a duration of tens of nanoseconds and wavelength of $1 \mu\text{m}$. When arriving at the depleted transport channel, the potential modulation of the SAW forms a train of moving QDs propagating through the surface-gate-defined rail. After loading an electron at the source QD, this SAW train allows to shuttle the electron through the quantum rail to a distant receiver QD [28, 29].

The robustness of a SAW train enables acousto-electric transfer of a single electron in a nanoscale circuit approaching macroscopic dimensions. An experimental investigation of a $22\text{-}\mu\text{m}$ -long SAW-driven single-electron circuit consisting of two tunnel-coupled channels – see single-electron circuit in Fig. 2a – achieved single-shot transfer efficiencies larger than 99% [31]. Here, the exact sending position within the SAW train is controlled via the delay of a picosecond-scale voltage-pulse trigger applied on the source QD. Adjusting the potential landscape in the tunnel-coupled wire (TCW), it is possible to partition the electron wave function via directional coupling at will between the two transport channels. Figure 2c shows an exemplary measurement of the single-shot transfer probability P as function of potential detuning Δ in the TCW. The partitioning data shows a constantly high transfer efficiency despite the detuning Δ of the TCW potential. The shape



of the partitioning data bears important information on the time-evolution of the flying quantum state that is of central importance for quantum applications.

To draw the right conclusions from the single-shot partitioning data, numerical simulations are essential. In the presently discussed example, time-dependent simulations of the electron's propagation through the TCW region, revealed charge excitation – as schematically shown via the potential landscapes shown in Fig. 2d – due to insufficient SAW confinement. In these calculations, the stationary potential is calculated with the *nextnano* software based on the true sample geometry and the electric properties of the heterostructure. Superposing this potential landscape with the dynamic modulation of the SAW, one can prepare an electron in its ground state and simulate its propagation through the device as shown in Fig. 2e. Setting a SAW-modulation as present in the experiment

($A \approx 17$ meV), the simulation shows a picture that is in good agreement with the experimental observation: As the electron enters the TCW, insufficient confinement within the moving, acousto-electric QD provokes charge excitation that prevents the appearance of tunnel oscillations. Instead, the probability to find the electron spreads according to the excitation spectrum. Unlike the experiment, numerical simulations allow to examine the effect of various device parameters in a systematic and fast way. For the presently discussed example, the time-dependent simulations particularly showed up the importance of the acousto-electric in-flight confinement. Augmenting the SAW amplitude by a factor of three ($A \approx 45$ meV), the time-dependent simulations predict preservation of quantum confinement at TCW transit resulting in tunnel oscillations [31]. Since an increase of the acousto-electric power of this scale is technically feasible, the time-dependent quantum simulation points out a central, easily addressable aspect in the realisation of electron flying qubits transported by sound.

Following the numerically guided pathway of augmented acousto-electric amplitude, we anticipate coherent in-flight manipulations of flying charge qubits on technically relevant length scales soon in single-shot experiments. For a flying qubit employing the electron's charge, first observations of tunnel-related probability oscillations have been already reported from experimental studies on SAW-driven transport of a continuous stream of single electrons [66, 67]. In congruency with the prediction of the aforementioned time-dependent simulations, the threshold of the SAW amplitude to significantly confine an electron in a single acousto-electric minimum was recently determined as $A = (24 \pm 3)$ meV in flight-time measurements [68]. For electron flying qubits defined by spin, increased SAW amplitude have already helped to demonstrate coherent transport of an entangled electron pair over 6 μm distance [69]. The coherent acousto-electric transfer of a single electron between remote quantum dots marks a new route to link quantum information in semiconductor qubit circuits where numerical simulations will certainly play a central role to identify key aspects and speed up experimental cycles.

2.2 Hot-ballistic electrons

On the contrary to the aforementioned acousto-electric transport approach, a lithographically-defined, but highly-tunable, quantum dot can also be employed to emit a single electron at high energy. These hot-electron sources for the controlled emission of single and multiple particles are of high interest from the perspective of higher-temperature operation and isolation from environment. In these devices, electrons can be emitted at an energy ~ 100 meV above the Fermi energy, hence the cooling of the Fermi sea at millikelvin temperatures may not be necessary. Besides, hot electrons can be transmitted through a depleted channel, eliminating undesirable interactions with the Fermi sea. For the controlled emission of single and multiple particles, hot-electron sources are driven by strong potential modulation determining the timing of electron emission via slow, stochastic tunneling through a barrier. This process has a potential advantage of a high purity, meaning that the energy and time window into which the particles (or wave packets) are emitted fluctuates little between successive emissions. On the other hand, due to a large phase space available, the inelastic scattering rate during propagation can be high, leading to short decoherence time.

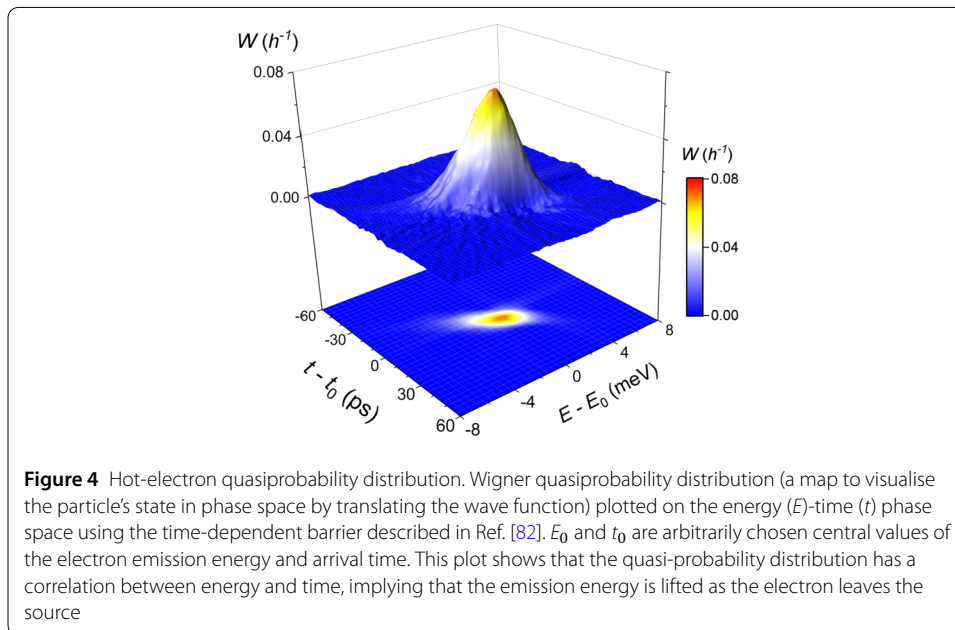
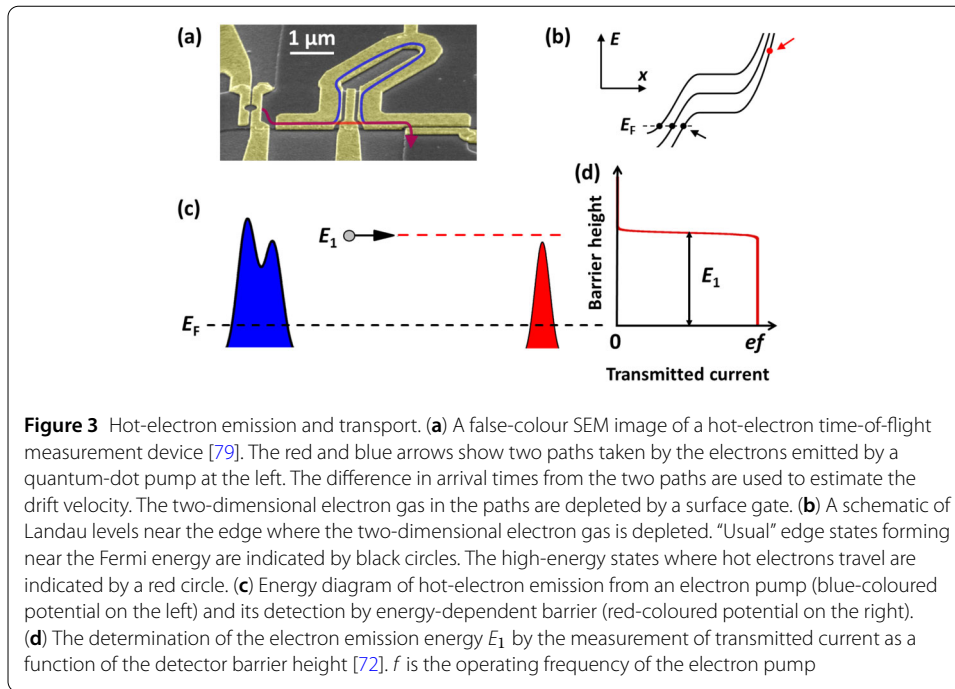
This is in contrast to the electrons confined in SAW potential or the Levitons, for which the electrostatic confinement or the limitation in available states (by the filled

Fermi sea), respectively, protect the states from scattering processes. The nature of inelastic processes for hot electrons injected in GaAs/AlGaAs heterostructures has been investigated in Ref. [70–76]. At zero or small magnetic fields, the dominant scattering process is electron–electron interactions by the Fermi sea. For low-energy electrons (a few tens of meV above the Fermi energy), the electron–electron interactions continue to be the dominant process at higher magnetic fields applied perpendicularly to the plane of two-dimensional electron gas. For high-energy electrons (~ 100 meV above the Fermi energy), the magnetic confinement to the channel edge limits the spatial overlap with the Fermi sea and consequently suppresses electron–electron interactions. Instead, the emission of longitudinal optical phonons [77] becomes the dominant process. Generally, the optical-phonon emission rate at high magnetic fields tends to be smaller than the electron–electron scattering rate at low magnetic fields, and therefore the ballistic transport length tends to be larger at higher magnetic fields. The suppression of backscattering processes due to chiral transport also contributes to a longer transport length at higher fields.

The technology to use hot electrons for electron quantum optics experiments is relatively new and not much information has been gathered regarding their suitability for applications in quantum information processing. In order to explore the potential to use these hot-electron sources for the preparation of flying qubits, it is important to gain very precise knowledge of the relevant properties of the injected particles. These are (i) the time- and energy interval into which particles are emitted (ii) the purity of the wave packets, namely the precision in the time- and energy-interval in which the particle is detected in every driving cycle. At the same time it is crucial to analyse, (iii) how these properties are affected during the propagation of wave packets along depleted channels and to minimise a possible deterioration of the signal. These aspects hence need to be tested and control over them has to be obtained.

The detection of hot-ballistic electrons emitted by a single-electron source was made using a scheme shown in Fig. 3 [72]. The energy distribution of hot electrons was obtained from the transmitted current through a detector barrier. In addition to the main distribution around the emission energy, replica of the distribution with discrete energy steps ~ 36 meV were experimentally observed. They were attributed to the emission of longitudinal-optical phonons. Further studies on phonon interactions [73, 74] led to a method to suppress phonon emission probabilities by softening the edge potential [75, 78]. This technique was used to extend the phonon scattering length to as much as ~ 1 mm. Using the long ballistic length, time-of-flight measurements were performed to extract the electron drift velocity ranging from 30 to 130 $\mu\text{m ns}^{-1}$ [79].

The time-of-flight measurements used a time-gating technique to measure the electron arrival-time distribution [80]. This was later developed into a tomographic measurement of quasi-probability distribution in the energy-time phase space by controlling the ramp speed of gate voltage [81–83]. This measurement revealed an energy-time correlation of the distribution imprinted by the ramp speed of source energy state during the emission process (see Fig. 4) [82]. The projection of this distribution onto the time or energy axis gives the arrival-time or energy distribution of the emitted states. The purity of the observed distribution was only 0.04, and therefore the observed state is likely to be a mixed state. We note that the time and energy resolutions of the experiment in Ref. [82] were estimated to be $\sigma_t \simeq 0.3$ ps and $\sigma_E \simeq 0.8$ meV, giving $\sigma_t \sigma_E \simeq 0.36\hbar$, implying that this



method is capable of resolving the minimum uncertainty limit ($\hbar/2$). Therefore the observed low purity is not due to poor measurement resolutions, but is likely due to noises in electron emission process from the source. In this set of experiments, the smallest arrival-time distribution observed was $\sigma_{t,\min} \simeq 5$ ps, and the smallest product of time and energy widths was ~ 30 times larger than the minimum uncertainty limit (taking into account the energy-time correlation). A method has been proposed in Ref. [84] to emit each electron into Gaussian-shaped minimum uncertainty states. Another important experimental technique is the full counting statistics of the electron number partitioned by a beam split-

ter (a tunnel barrier). This has been demonstrated using noise measurements [85] or a trap coupled to a single-charge detector [32, 86].

The time scale of electron emission is directly reflected in the width of the emitted wave packets. In quantum optics experiments with electrons, this time scale is important for the visibility of interference effects. In order to obtain these insights, the times at which single or multiple particles are emitted from the hot-electron sources can be studied analytically or numerically taking into account the time-dependent modulation of the single-particle energy levels, as well as of the shape of the tunneling barrier between quantum dot and conductor [80]. Importantly, theoretical studies have recently shown that Coulomb interaction between electrons on the dynamically driven quantum dot have a strong impact on the energies at which the particles are emitted. Most crucially this impact on the electron energies also directly influences the time scale on which the emission of the different particles takes place [87]. This theory furthermore predicts that the separation of time scales becomes particularly relevant for energy-dependent barriers [88]. Different schemes of how to read out these different relevant *emission* time scales using side-coupled detector dots [89] or nonadiabatic pumping schemes [90] have been suggested. This last scheme in particular also addresses relaxation times due to phonons during the *emission* process.

Based on the work described above, one can expect that realisations of Mach–Zehnder experiments will become possible with these types of sources, as suggested in Ref. [91, 92], similar to previous proposals for single- and two-particle interferometers for minimal-excitation single-particle sources [93–95]. Ref. [92] studied phase-averaging effects, which are particularly important for the temporally-short, high-energy single-electron wave packets. As a result it becomes necessary to tune asymmetric interference arm lengths and delay time, which could be achieved by tuning the drift velocity. These analytical studies [91–95] assume an emission of pure states and ideal beam splitters, which are over-simplified compared to a realistic experiment. Hence, in order to improve the device characteristics, more realistic numerical modelling of these aspects could be a helpful complement. While the electron coherence of hot electrons is yet to be demonstrated, the short length of electron wave packet in time domain and the ability to control their emission timing with a picosecond resolution can be useful in ultrafast electronics applications. In-situ voltage sampling under cryogenic environment has been demonstrated with a bandwidth potentially exceeding 100 GHz [96]. This technique was used to determine the precise gate voltage ramp profile for quantum tomography measurements [82].

2.3 Leviton qubits flying over the Fermi sea

A conceptually different approach to realise an electron flying qubit is to generate a single-electron wave packet directly from the Fermi sea. This approach seems counterintuitive as a perturbation of the Fermi sea excites both electrons and holes and does in principle not allow the generation of a *pure* single-electron wave packet. L.S. Levitov and co-workers came up with an original idea to form a collective electron excitation flying over the Fermi sea without leaving a hole [97–99]. It has been shown that a voltage pulse of Lorentzian shape:

$$V(t) = \frac{V_0}{\pi} \frac{\tau/2}{t^2 + (\tau/2)^2} \quad (2)$$

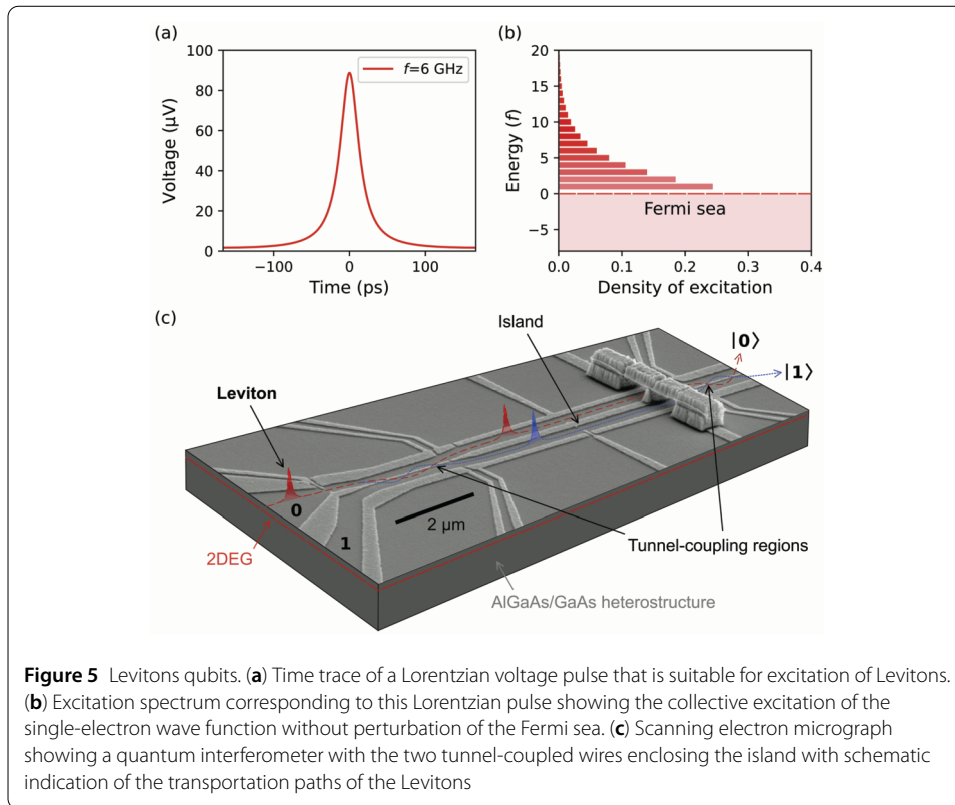


Figure 5 Levitons qubits. **(a)** Time trace of a Lorentzian voltage pulse that is suitable for excitation of Levitons. **(b)** Excitation spectrum corresponding to this Lorentzian pulse showing the collective excitation of the single-electron wave function without perturbation of the Fermi sea. **(c)** Scanning electron micrograph showing a quantum interferometer with the two tunnel-coupled wires enclosing the island with schematic indication of the transportation paths of the Levitons

generates a *pure* single-electron excitation – the so-called Leviton – if the amplitude V_0 and the full-width at half-maximum τ are chosen to match the quantization condition:

$$\int_{-\infty}^{\infty} eV(t) dt = h, \quad (3)$$

where e is the elementary charge and h is Planck's constant. A Lorentzian pulse fulfilling this quantization condition is shown in Fig. 5a. Figure 5b shows the corresponding excitation spectrum – meaning the occupation of states above and below the Fermi energy. The calculation shows a distribution that is characteristic for Leviton excitation. The collective wave function is only occupying the states right above the Fermi level (zero energy) forming a *pure* electronic excitation that is robust against relaxation.

It took almost 20 years until the theoretical concept of a Leviton was demonstrated in experiment [30]. The reason for this long delay was mainly related to the difficulty in generating clean and sufficiently short voltage pulses of Lorentzian shape that are injected directly via an Ohmic contact of the quantum device. Compared to the aforementioned quantum-dot-based sources, the Leviton approach brings the advantage that nanolithography techniques are not required to define single-electron emitters. At last, progress in microwave engineering has bridged this gap and allowed one to verify this original concept. The experiment demonstrated minimization of shot noise due to the absence of holes via Leviton formation and Hong–Ou–Mandel type experiments with very high degree of indistinguishability. To study the wave function of such flying charge excitation [99–106], quantum tomography protocols have been developed allowing a measurement of the Wigner distribution function [61, 62, 107, 108]. In addition, time-resolved

experiments have shown propagation of Leviton-like flying charges over distances of more than 80 μm without measurable dispersion [53]. Owing to the occupation of states right above the Fermi sea, Levitons are expected to have extremely good coherence properties [109–112] compared to other injection schemes [113–115] making them highly promising candidates for electron-flying-qubit implementations.

The next important step to benchmark these benefits is the implementation of a quantum interferometer with Levitons. Since Levitons are simply injected via voltage pulses on an Ohmic contact, the geometry of such a single-qubit device is very similar to that of early experiments [42]. Figure 5c shows an SEM image of a possible implementation with schematic indications of the interferometer paths. The propagation velocity of the injected Leviton pulse is expected to be on the order of $100 \mu\text{m ns}^{-1}$ [53]. Since the dynamics of such propagating pulses within a quantum interferometer have not been investigated yet, it is important to have experimental control of the pulse width to fit the flying charge excitation within the tunnel-coupling regions ($\approx 2 \mu\text{m}$) requiring pulses with full-width-at-half-maximum smaller than 20 ps. The generation of such pulses with cutting-edge microwave synthesis approaches is possible but at the technical limit. A promising alternative route allowing pulses with widths of 1 ps or smaller is the optoelectronic generation via ultrafast photo switches [116–120]. Besides a proper Leviton source, it is of utmost importance to design a quantum interferometer structure allowing for qubit manipulation with maximum efficiency. For this purpose, numerical simulations serve as a useful tool to model the evolution of quantum states along the interferometer structure. In order to deduce the coherence length of a certain implementation it is necessary to measure the strength of the quantum oscillations for devices with successively increasing island-length. The knowledge on these aspects of a single electron flying qubit made up by Levitons will be decisive for the applicability in quantum-computing implementations.

One route to realise flying qubits based on Levitons employs electronic waveguides defined by surface gates in the 2DEG of a GaAs/GaAlAs heterostructure [42, 53]. An alternative platform is transport along quantum Hall edge channels [25, 41]. It is formed when a 2DEG is placed in a very large magnetic field. In this regime the bulk becomes insulating and the only quantum channels carrying the current occur on the sample edge. It is applicable in the aforementioned GaAs framework or lightly doped graphene. The implementation of quantum point contacts (QPCs) enables the realisation of an electronic beam-splitter. By combining two QPCs, an electronic Mach–Zehnder interferometer is realised [25, 121] allowing full qubit manipulation on the Bloch sphere. Being chiral, the propagation along quantum edge channels offers a very long mean free path and coherent transport [43]. In this regime, all the electron quantum optics tools are realizable such as Hanbury-Brown–Twiss [122] and Hong–Ou–Mandel interferometry [54]. Single electron sources based on Levitons have been also implemented, particularly in graphene [123, 124]. Compared to quantum wires based on electronic waveguides at low magnetic field, the advantage is a nearly perfect free propagation of electrons, thanks to the chiral nature of the edge channels (electrons cannot go back after scattering on impurities). The drawback is the use of few Tesla magnetic fields and the chiral nature of the propagation which makes coupling of more than two electron flying qubits challenging.

Single-shot detection represents a major task to realise an electron flying qubit with Levitons. For the aforementioned investigation of quantum oscillations, statistical measurements are sufficient. In order to control single Leviton qubits individually, it will be

however necessary to detect the presence for each flying electron via capacitive coupling to an ultra-sensitive quantum detector. One possible implementation of such a quantum detector is a spin qubit that is operated in a regime where it is extremely sensitive to charge fluctuations [125]. At present, this type of detector is capable of sensing a few electrons and enables a quantum non-demolition measurement [126]. The quantum detector is able to record the presence of a passing flying electron without perturbing its quantum state that can in turn be reused after detection for further quantum manipulations. This aspect is an important advantage over single-photon detectors where the photon disappears after detection. Another possible implementation that has been put forward recently guides the flying electron through a meander structure which is capacitively coupled to two large metal electrodes. The passage of the flying electron beneath the two surface electrodes generates an oscillating voltage signal. This detector is expected to have a sub-electron sensitivity [127] and, when properly integrated into a quantum circuit, can also be adapted for quantum non-demolition measurements.

Another aspect of major importance is the scalability of surface-gate-defined quantum-interferometer devices. Figure 6 shows an SEM image of a prototype multi-qubit implementation hosting four quantum interferometers. Simultaneous operation of the electron flying qubits is accomplished via an extended bridge cross-connecting island-gate of each device. To implement a two-qubit gate in such a setup the Coulomb interaction of flying electrons is exploited. Let us consider the case where two Levitons are simultaneously sent through a pair of neighboring quantum interferometers. By adjusting the potential barrier of a Coulomb-coupling gate (C) – as shown in Fig. 6 – the flying electrons are exposed to their respective Coulomb potential which introduces a quantum phase ϕ causing entanglement. The phase induced by each of the two electrons is proportional to the coupling constant and the interaction time, hence to the gate length. The Coulomb-coupling strength can be adjusted by changing the gate voltage on the electrostatic gates defining the phase-exchange window. The coupling region can be as short as 1 μm for the case of ballistic electrons [128, 129] and much shorter for the case of SAW-transported electrons

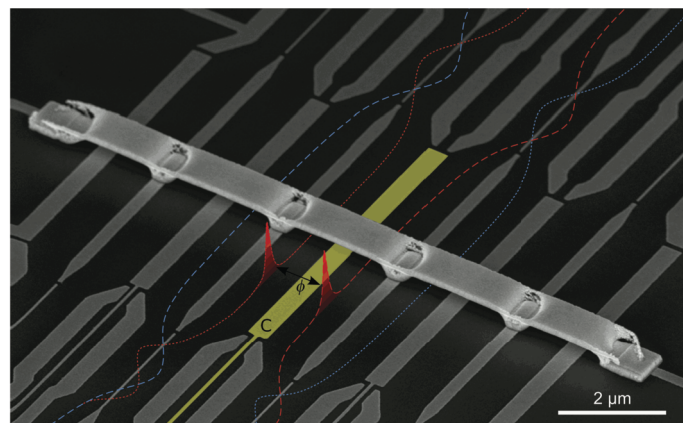


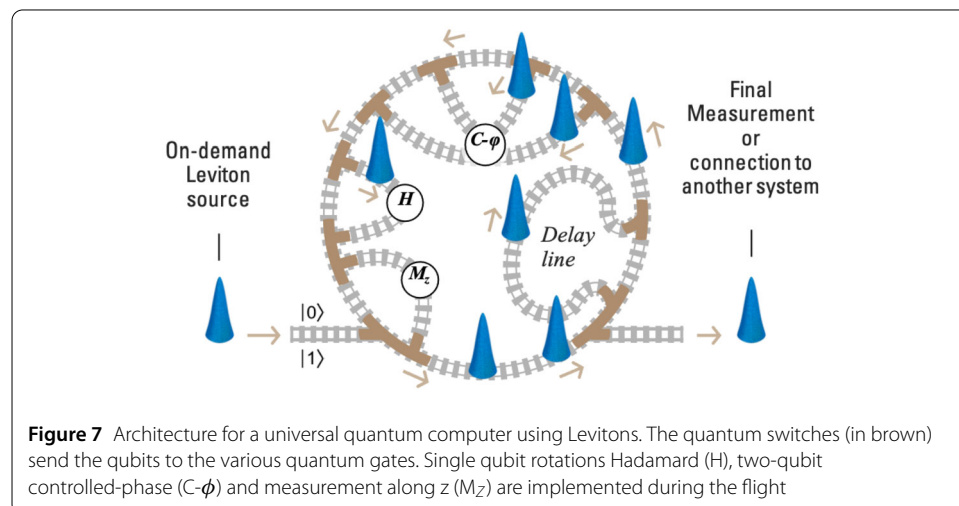
Figure 6 Scanning electron microscopy image of a multi-qubit flying electron architecture. The image shows four quantum interferometers that can be simultaneously operated owing to a common bridge that connects the islands of each device. The dashed lines schematically indicate the paths of two Levitons in two neighboring interferometers. The intermediate gate C (highlighted in yellow) allows for controlled Coulomb coupling of the Levitons and thus in-flight entanglement

since the propagation speed is 100 times smaller. If a π phase shift is induced, the probability of detecting an electron in the output port $|0\rangle$ or $|1\rangle$ is inverted, hence realising a controlled phase gate C_ϕ . Combining this experimental setup with two interferometers one can even go one step further and test Bell's inequalities as proposed in references [7, 130]. In this case, all of the four beam splitters are used and a π phase shift is induced with the Coulomb coupler enabling the formation of a maximally entangled Bell state. The scalability of electron-flying-qubit implementations is very similar to that of photonic circuits where multiple Mach–Zehnder interferometers are connected in parallel and series [131].

The central challenge to build a quantum computer is to scale up a qubit system. For the latest technological stage, millions of physical qubits would be required [132]. This scalability problem is inherent to any qubit that needs to be addressed individually via an external parameter such as a gate voltage or a laser. Important issues to be solved on the way to build a universal quantum computer are presently the improvements of the fidelity of the qubits as well as their connectivity [133].

Electron flying qubits using Levitons could allow one to implement an original architecture to build a universal quantum computer as schematized in Fig. 7. Although the architecture of Fig. 7 is a theorist view at this stage, it has very appealing features, in particular the fact that it is structurally different from the mainstream approach that uses localized qubits. Indeed in the mainstream approach, the hardware corresponds directly to each qubit: for instance for spin qubits, one needs a certain number of electrostatic gates per qubit to confine the electron, address it with microwaves and eventually measure its state. It follows that the hardware footprint is proportional to the number of qubits. In contrast, in this 'synchrotron-like' quantum computer, the flying qubits are stored in a loop and fast quantum routers are used to bring them to single-qubit gates, two-qubit gates, delay lines or measuring apparatus [134]. Hence, the hardware footprint can in principle be extremely small: a few quantum routers (one per type of gates or measurement) are sufficient to control an arbitrarily large number of qubits. The Leviton qubits are created on demand and one only needs a loop, which is large enough to hold Levitons while they go around it.

The second, perhaps more important, advantage of this architecture is the connectivity of the two qubit gates: using the delay line shown in the schematic, one could move the



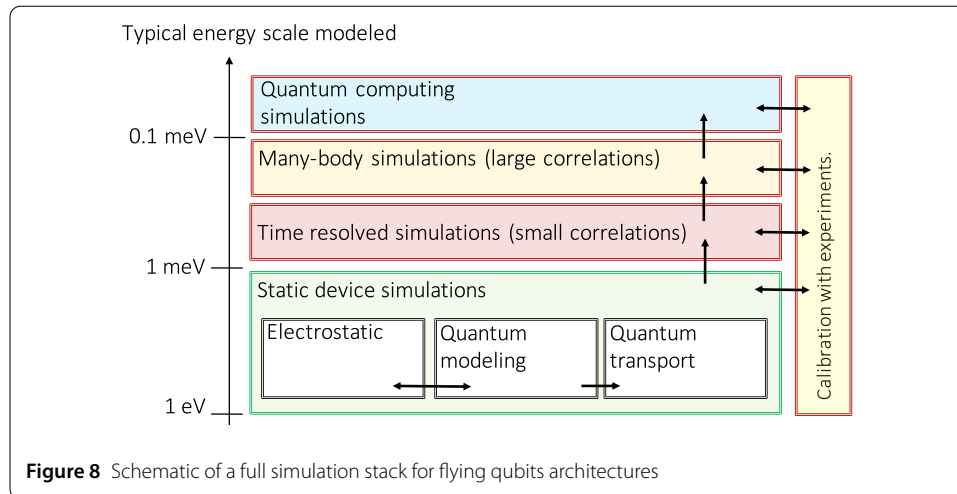
qubits so that any pair of flying qubits could be put next to each other and, hence, one could apply two qubit gates between any pair of qubits. This is again in contrast to the mainstream approach where each qubit being localized, it can only interact with a few other qubits, usually its nearest neighbours. Such a dramatic increase in connectivity could have deep consequences to reduce the overhead of quantum error correction and fault tolerant operations.

Another advantage of the flying qubit architecture for quantum computing is that qubits can easily be recycled: old qubits can be expelled from the loop and fresh ones incorporated while ancilla ones can be used to calibrate or test the various parts of the circuit in order to isolate and retune sections that are not performing correctly. This flexibility could again be very instrumental in quantum error correction in order to get rid of rare lethal errors. Indeed, in quantum error correction, not all errors are equal; some, even if rare, are lethal to the calculation [135]. In this respect, a long-term advantage of the flying qubit architecture is the possibility to correct these rare errors. Altogether a functional flying qubit technology could make quantum error correction affordable, bringing the millions of qubits which are required to build a fault tolerant quantum computer down to tens of thousands. Alternatively, the electron-flying-qubit approach could be used to complement other approaches by providing a ‘quantum bus’ that implements the missing long-range coupling between distant localised qubits. Experimentally, we are still in the early stage of the development of such an electron-flying-qubit platform. Yet, it is very interesting and appealing to see that it leads to a conceptually very distinct object from the localized qubit approach. This means in return that there is a lot of room for a new architecture to be invented to bypass the intrinsic limitations of the ones that are pursued so far.

To end this section on the experimental progress on electron flying qubits realised in semiconductor devices, we would also like to point out promising approaches to manipulating single electrons on other unique platforms. Alternative to the here-described semiconductor devices, single electrons can be confined on the surface of liquid helium [136–139] or rare earth atoms such as neon, argon or krypton [140]. These systems provide a two-dimensional electron system with ultra-high mobility and strong Coulomb interaction. Similar to SAW-driven single-electron transport discussed in Sect. 2.1, electrons on the surface of liquid helium can be transported with very high precision through coupling to an evanescent piezoelectric SAW [139]. Besides that, electrons can be attracted to the surface of a solid crystal made from rare-earth atoms in vacuum. For the case of a solid neon substrate, a single electron has been trapped with electrostatic gates and coupled to a superconducting microwave resonator [140]. This allowed to observe coherent coupling of motional electron states to a single microwave photon with coherence properties similar to state-of-the-art charge qubits [141].

3 Numerical modelling of quantum devices

Numerical simulations play an important role in the development of quantum computing architectures and the flying qubit platform is no exception. Achieving a full stack of numerical tools to compute and predict the various properties of the devices is key to certify that the devices behave as they are supposed to and allows one to eventually optimise their behaviour. Figure 8 shows a typical stack that is being developed for flying qubit architectures. At the bottom are the device simulations that incorporate the material modelling as well as the geometry of the device. These are usually performed at the self-consistent



electrostatic quantum level, i.e. the electrostatic problem is solved simultaneously with the quantum problem associated with the active part of the device (typically the region around the GaAs/AlGaAs interface in the devices discussed in this article). The self-consistent potential can be used by quantum solvers to calculate the quantum transport properties of the device, e.g. the conductance or the current noise or other observables. Those properties can be directly compared to DC experimental measurements to obtain a direct feedback on the quality of the modelling and its calibration. The proprietary *nextnano* [142] platform or the open-source KWANT software [143] are complementary tools that can be used for this stage.

Once the static properties are well understood, one can proceed to simulate the propagation of the electron flying qubits, including voltage pulses and the associated Levitons, in real time. The TKWANT extension [144] of KWANT provides the necessary environment for such simulations (e.g., to study the role of Coulomb repulsion at the time-dependent mean field level). The next level is a proper treatment of many-body effects aiming to account for e.g. interactions between different Levitons or various relaxation and dephasing mechanisms (such as one electron decaying into two electrons and one hole). We note that there are no general purpose simulation approaches that can handle this problem in a “blackbox” way. At the top of the stack are “pure” quantum computer simulators where the actual underlying physics has been hidden and one simulates only the effective dynamics of the computational degrees of freedom (potentially with some extra noise or dissipation terms to account for the actual limitations of the devices). As indicated by the arrows on the schematic, the different parts of the stack provide parameters to calibrate the other levels. As one goes up the stack, one usually must give up some microscopic details in order for the computations to remain affordable. Therefore, the calibrations must be done with care for the errors not to accumulate. Below, we focus at first on the static simulation part of the stack with a special emphasis on the calibration of the simulations with respect to the experiments and on the modelling of real nanodevices. At the end of this section, we briefly address time-resolved and many-body simulations.

3.1 Static quantum mechanical simulations

Tuning a single qubit into optimal operation is so far a tedious task. An attempt to find such conditions trying various setups at random is time and resource consuming. In order

to go easier beyond experimental proof of concept (also known as Technology Readiness Level (TRL) 3), it is thus crucial being able to predict the viability of a certain sample design prior to its physical realisation. As outlined above, precise potential calculations combined with dynamic quantum mechanical simulations are playing a key role in this regard enabling validation of electron-flying-qubit technology in the lab (TRL 4). Being able to predict the reliability of a certain sample geometry paves the way to implement and setup electron flying qubits in a reproducible manner – enabling validation of the technology in a demonstrative or even commercial setting (TRL 5 and 6).

Since the basic elements of the electron flying qubits (interconnects, TCWs and interferometers) are exploiting to a great extent single-particle physics, they require high-quality quantum mechanical simulations for one electron in complicated electrostatic potentials. The necessary information is obtained from a numerical solution of the stationary Schrödinger equation, see Eq. (4) below. The precise solution can be found by using a platform such as the nextnano software. Its advantages include the possibility to adapt the numerical procedure for different materials, various geometries of the nanoconductors and shapes of the gate-induced potentials.

Let us review the basics of the static quantum mechanical simulations, some features of the nextnano tools, and provide examples of how these tools can be used for calibration of the experiments and engineering the nanodevices.

3.1.1 Basic equations and methods of static single-particle simulations

Basic targets of the static quantum mechanical simulations include the study of the shape of electron wave functions and the energy-dependent transmission through one nanounit and through the entire circuit [145–147]. The transverse profile (i.e. along the direction being perpendicular to the propagation direction) allows one to judge whether the quantum wires are close to the desirable setup and to control, e.g., the absence (presence) of tunnelling between two isolated (coupled) wires. Ballistic transmission of the electron through the circuit is even more important. When various units are connected, there are always spatial inhomogeneities which can result in reflection of the propagating electron. The reflection hinders the flying qubits from their normal operation and must be minimised as much as possible. To this end, one can numerically find an energy corresponding to transparency windows for a realistic circuit and to work further in a vicinity of this special energy range.

The quantum mechanical system can be modeled at different levels of approximations that range from a semi-classical description to an effective mass approximation to a multi-band $k \cdot p$ model. Considering conduction-band electrons within the single-band approximation, the envelope wave functions, ψ_n , are solutions of the stationary Schrödinger equation

$$\hat{H}\psi_n(\mathbf{x}) = E_n\psi_n(\mathbf{x}), \quad (4)$$

where \hat{H} is the Hamiltonian operator of the closed quantum system, E_n are the energy levels defining the energy spectrum of the system, n are quantum numbers marking different single electron quantum states, and $\mathbf{x} = (x, y, z)$ is the space coordinate. The Hamiltonian operator

$$\hat{H} = \epsilon(\hat{\mathbf{p}}) + V(\mathbf{x}) \quad (5)$$

is the sum of a kinetic energy operator $\epsilon(\hat{\mathbf{p}})$ and a potential energy $V(\mathbf{x})$, where the electron momentum operator is defined in the standard way as $\hat{\mathbf{p}} = -i\hbar\nabla$. Here, $\epsilon(\hat{\mathbf{p}})$ is the dispersion relation describing the momentum dependence of the electron energy which accounts for all effects governed by the crystalline lattice, and $V(\mathbf{x})$ is the inhomogeneous potential in which the electron propagates. $V(\mathbf{x})$ contains the electrostatic potential and conduction band offsets at material interfaces. For example, in the simple case of a homogeneous isotropic material where the electrons move almost freely, one can use the effective mass approximation which yields $\epsilon(\mathbf{p}) = (p_x^2 + p_y^2 + p_z^2)/2m^*$, where m^* is the effective mass of the electron in the material.

The potential $\phi(\mathbf{x})$ describes the electrostatics within the system and is the solution of the Poisson equation

$$\nabla \cdot [\epsilon(\mathbf{x})\nabla\phi(\mathbf{x})] = -\rho(\mathbf{x}), \quad (6)$$

where $\epsilon(\mathbf{x})$ is the material-dependent permittivity, and $\rho(\mathbf{x})$ is the charge density throughout the system. This charge density is given by

$$\rho(\mathbf{x}) = e[-n(\mathbf{x}) + p(\mathbf{x}) + N_D^+(\mathbf{x}) - N_A^-(\mathbf{x})] + \rho_{\text{fixed}}(\mathbf{x}), \quad (7)$$

where $n(\mathbf{x})$ and $p(\mathbf{x})$ are the electron and hole densities, and $N_D^+(\mathbf{x})$ and $N_A^-(\mathbf{x})$ are the ionized donor and acceptor concentrations, respectively, e is the (positive) elementary charge, and $\rho_{\text{fixed}}(\mathbf{x})$ contains immobile space or surface charges.

Here, the electron density $n(\mathbf{x})$ explicitly depends on the energy levels E_n and envelope wave functions ψ_n from Schrödinger's equation, Eqs. (4),(5). For a finite system at equilibrium, the electron density is given by

$$n(\mathbf{x}) = \sum_n \frac{2|\psi_n(\mathbf{x})|^2}{1 + \exp((E_n - E_F)/k_B T)}, \quad (8)$$

where E_F is the Fermi level (or chemical potential), T is the temperature, and k_B is the Boltzmann constant. Thus, the electrostatic potential $\phi(\mathbf{x})$ depends on the energy levels E_n and wave functions ψ_n , but also enters the Schrödinger equation, Eqs. (4),(5), as part of the potential energy operator $V(\mathbf{x})$. This shows that the Schrödinger equation and Poisson equation (Eq. (6)) are coupled and need to be solved self-consistently.

The self-consistently obtained spectrum and wave functions can be used further to calculate quantities which explain and describe quantum transport through various nano-devices connected to external leads. Two such quantities are (i) the partial local density of states (pLDoS), $n(x, y, E)$, and (ii) the energy dependent transmission, $T_{ij}(E)$. The pLDoS is the probability to find in a given space-point the propagating electron which has a given energy, E , and has been injected in a given lead. We note in passing that the local density of states is the sum of the pLDoS over all leads. Hence, the coordinate dependence of pLDoS illustrates how the electron with a given energy propagates through the device [148]. The energy dependent transmission, $T_{ij}(E)$, is determined by the probability for the electron which is injected into lead i to reach lead j .

The pLDoS and the transmission from one lead to another can be found by using the retarded Green's function, $\hat{G}^R(E) = ([E + i\alpha]\hat{1} - \hat{H})^{-1}$ where E is the electron energy and

$\alpha \rightarrow 0^+$ is a mathematical regularizer which reflects the retardation of the physical response (see Ref. [148] and Ref. [149] for details). In the space-coordinate representation, the coordinate-dependent Green's function can be expressed via the wave functions and the spectrum (the so-called spectral and Lehmann representations). Hence, the solution of the Schrödinger equation provides the input needed for the theoretical study of transmission.

The transmission provides valuable information on quantum interference occurring in the TCW or the Aharonov–Bohm (AB) interferometer. In the original setup, the AB interferometer involves the magnetic field, $\mathbf{B} = \text{curl}\mathbf{A}$, which can be included into the study as a shift of the momentum operator by the vector potential, $\hat{\mathbf{p}} \rightarrow \hat{\mathbf{p}} - e\mathbf{A}$. In practice, a magnetic field variation is too slow on the time scales needed for qubit operation, so electrostatic manipulation of the gates is much more practical. Nevertheless, for optimisation of the design, experiments and simulations in the presence of a magnetic field are still useful.

Schrödinger's equation can only be solved analytically for some specially chosen potentials, whereas, in the general case, spectra and wave functions can only be found numerically. The numerical solvers are applied after discretization, which means that the continuous space is reduced to points on a grid and derivatives are substituted by differences. Here, the grid spacing is an important parameter which controls the accuracy of the numerically obtained answers. In our qubit devices, layer structures and dopant distributions create a triangular shaped quantum well along the substrate growth direction. In this quantum well, quantum confinement effects cause the electrons to form a two-dimensional electron gas which is modulated in the two directions perpendicular to the substrate growth direction in accordance with the influence of the gate geometries. For such 3D devices where thousands of eigenstates have to be taken into account, efficient solvers for the Poisson and Schrödinger equations such as preconditioned conjugate gradient for Poisson and Arnoldi iteration for Schrödinger are mandatory in order to overcome the huge computational costs. Moreover, achieving self-consistency between the Poisson and the Schrödinger equation is not easy and requires the use of special techniques such as predictor–corrector methods [150] in order to robustly obtain solutions. In strongly non-linear regimes such as in the quantum Hall regime, other techniques such as Ref. [151] might be needed.

As we have already mentioned, the simulation of quantum transport and thus obtaining the pLDOS and the transmission requires the use of Green's function techniques [152], which are computationally extremely expensive in the most general case. Fortunately, the ballistic limit of quantum transport suffices for the accurate description of flying qubits. This allows the so-called Contact Block Reduction (CBR) method [149, 153] to be used here in order to reduce the computational cost down to a point that even large three-dimensional devices of arbitrary shape and with an arbitrary number of contacts can be easily modelled.

3.1.2 *The nextnano software and its applications for engineering flying qubits*

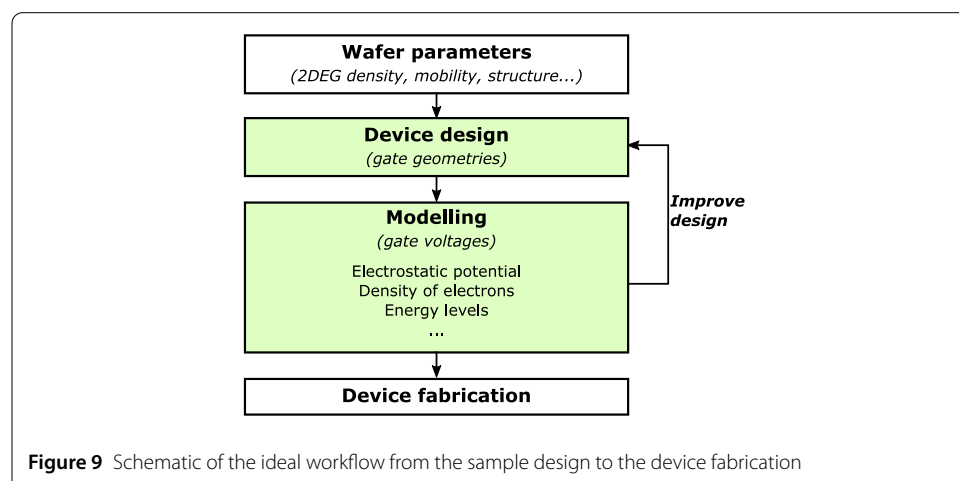
Starting from the year 2000, the nextnano software had been developed at the Walter Schottky Institute of the Technische Universität München. Later, it resulted in the spin-off company nextnano GmbH. The software, which is now further developed by this company, is a user-oriented platform meant for modelling various semiconductor-based nanodevices, cf. Refs. [142, 154, 155], including optoelectronic elements and qubits.

The main focus is on the simulation of the quantum mechanical properties of such devices. The nextnano's core product, the nextnano++ software [142], is a 3D Schrödinger–Poisson–Current/CBR solver for nanotransistors, LEDs, laser diodes, photodetectors, quantum dots, nanowires, solar cells and qubits. The second product, nextnano.NEGF [152], is a quantum transport solver targeting quantum cascade lasers and resonant tunneling diodes. The nextnano software (including its early versions) has been successfully used to optimise the design of semiconductor-based (charge and spin) qubits [156–161]. Below, we focus on several important applications of this software for engineering the electron flying qubits.

Appropriate models for quantitative simulations: Quantum devices made from GaAs semiconductor heterostructures can easily be engineered by proper design of the gate geometry. To ensure the best performance of the electronic device – that is to find the most suitable gate geometry – it is crucial to know the exact electrostatic potential landscape generated by the electrostatic gates. This requires to take into account the material parameters such as 2DEG density and mobility, dopants concentration, induced surface charges, etc.

Traditionally, the workflow to determine the optimum gate geometries for a given heterostructure has been an iterative process between device fabrication in clean room facilities and low-temperature characterisations. This is immensely time consuming and resource demanding. The ideal workflow is presented in Fig. 9 where the iterative process takes place mainly at the modelling stage, *before* the device fabrication.

To find an accurate model for quantitative simulations, Chatzikyriakou *et al.* [162] developed a model using the nextnano software and benchmarked it with experimentally measured QPCs with a wide range of geometries. They assumed a layer of surface charges and a spatially uniform doping concentration, both having a frozen ionization state due to the very low temperatures at which the experimental measurements are taken [31, 163]. First, 1D simulations of GaAs/AlGaAs heterostructures (Fig. 10a), with a Schottky gate on top, are employed in order to deduce the doping concentration such that the simulation reproduces experimentally measured characteristics of these heterostructures that exist on the chip that hosts the QPCs. These structures are covered by metal electrodes that are very large compared to the QPC gates (>500 nm in each Cartesian direction) and that are finally connected to the QPC gates. Then, removing the gate from the simulated het-



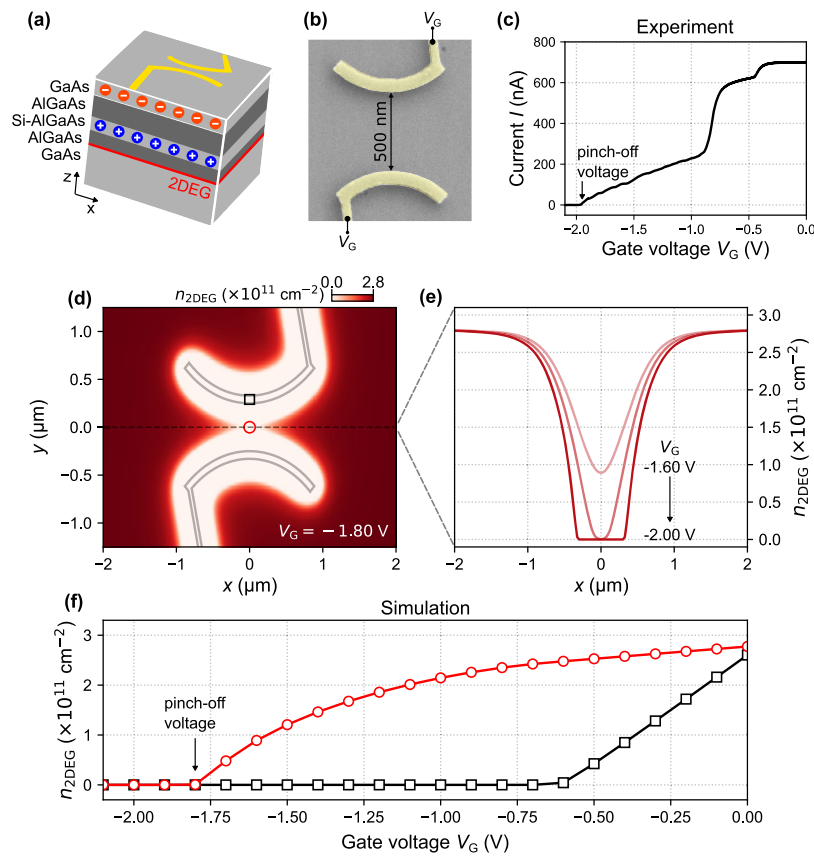


Figure 10 Calibration details. (a) Schematic of the GaAs/AlGaAs heterostructure below the surface-gate defined QPC (yellow) with indications on the surface charges (red circles), Si dopants (blue circles) and the 2DEG (red line). (b) Scanning-electron-microscopy image of a QPC design. (c) Experimental current / across the narrow constriction as a function of the surface-gate voltage V_G . (d) Simulated distribution of the electron density $n_{2\text{DEG}}$ for $V_G = -1.80$ V using nextnano. The grey polygons correspond to the gate geometry. (e) Electron density $n_{2\text{DEG}}$ along the constriction ($y = 0$; dashed line in (d)) for three values of V_G . (f) Electron density $n_{2\text{DEG}}$ below the surface gate (black square) and at the middle of the constriction (red circle). The simulated QPC pinch-off occurs when the 2DEG is completely depleted

eroheterostructure, the surface charges are adjusted so that the 2DEG electron density is equal to that taken from Hall measurements on the same wafer, at $T = 4.2$ K (frozen surface states). To simulate the region where electron transport takes place, 3D simulations are carried out with the exact gate geometry of the quantum device. These gate geometries are directly imported from the computer-aided design (CAD) layouts (standard files in GDS format) using the open-source Python package nextnanopy [164].

Figure 10 shows a typical example of electron depletion in the 2DEG when applying a gate voltage to the electrostatic gates that face each other. When a small negative voltage is applied, the electron density under the gates is first depleted, forming only a narrow 1D constriction in the center of the two gates. Reducing further the voltage, the 1D channel is completely depleted and the transport channel is *pinched-off*. The simulation shows a remarkable agreement with the experimental pinch-off value ($V_G = -1.8$ V).

In the same spirit, one can use such simulations to calculate the potential variations seen by the electrons within the 2DEG. An example of a complex quantum device with a tunnel-coupled wire from Takada *et al.* [31] is shown in Fig. 11. Using the exact gate ge-

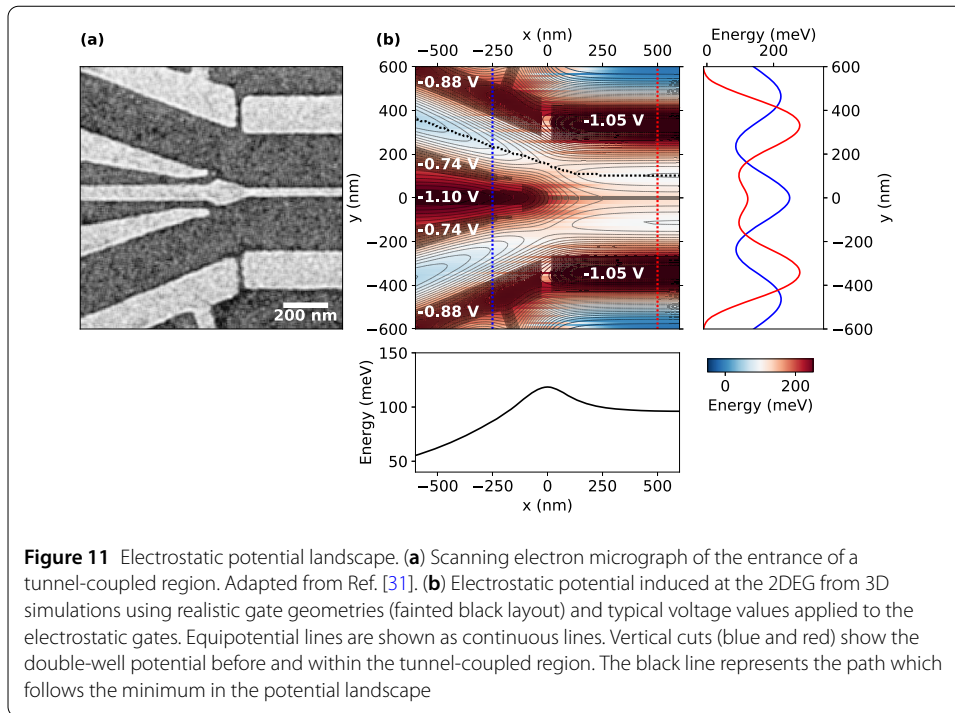
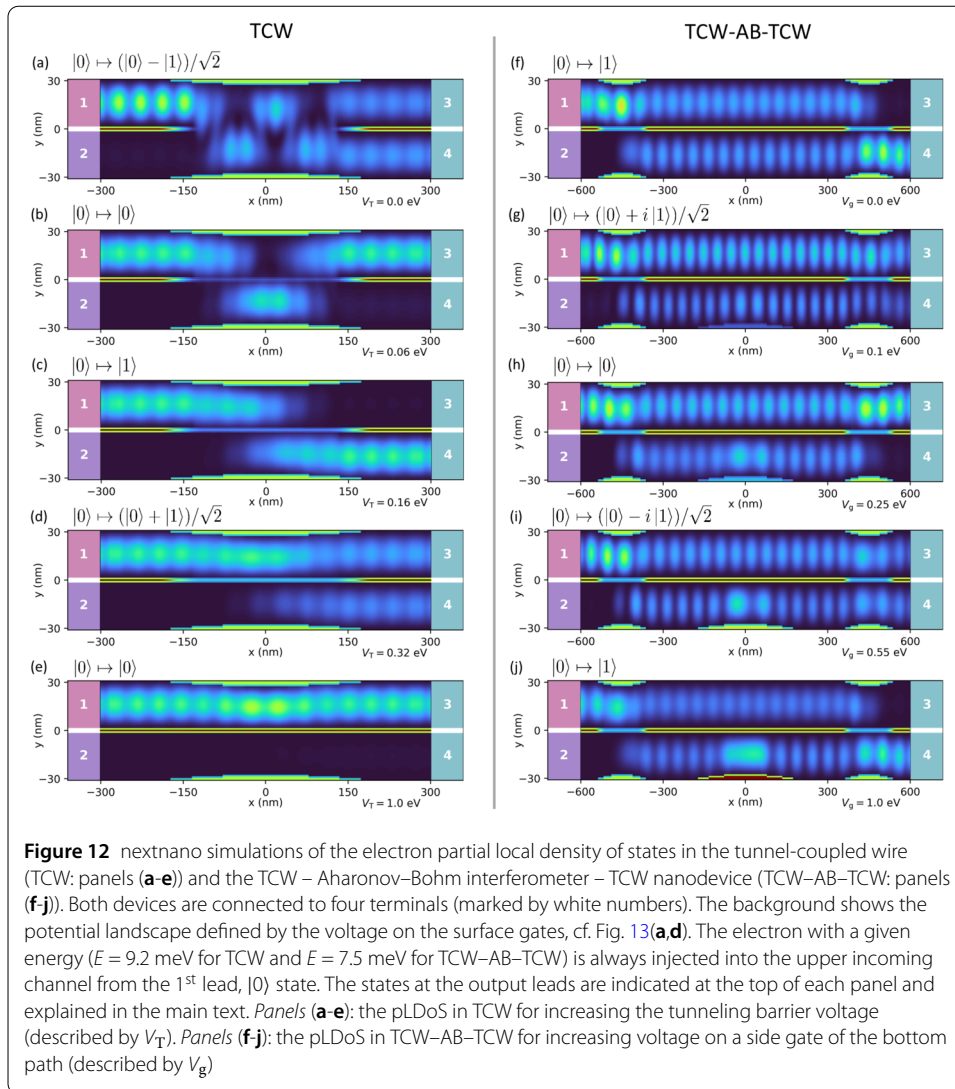


Figure 11 Electrostatic potential landscape. **(a)** Scanning electron micrograph of the entrance of a tunnel-coupled region. Adapted from Ref. [31]. **(b)** Electrostatic potential induced at the 2DEG from 3D simulations using realistic gate geometries (fainted black layout) and typical voltage values applied to the electrostatic gates. Equipotential lines are shown as continuous lines. Vertical cuts (blue and red) show the double-well potential before and within the tunnel-coupled region. The black line represents the path which follows the minimum in the potential landscape

ometries and voltages from the experiment, the electrostatic simulations reveal the variation of the potential along the path which an electron would follow before entering the tunnel-coupled region (black line). In these experiments, the single electron is excited to higher energy states which were attributed to the abruptness in the potential landscape at this location. This undesired excitation could be mitigated by optimising the device geometries thanks to quantitative modellings.

The shape of the electrostatic potential in the 2DEG plane is input to further calculations of the energy-dependent transmission function which corresponds to the probability that an electron is reflected or transmitted along the different paths in the flying qubit structure. One-dimensional cuts through this potential in the uncoupled wires (blue) and within (red) the tunnel-coupled regions are shown in Fig. 11b. One can see parabolically shaped double-well confinement potentials, cf. Fig. 1c. Such potentials and the interplay between symmetric and anti-symmetric states with respect to the direction perpendicular to the propagation direction have been analyzed numerically in Ref. [145] where detailed features of the transport measurements such as in-phase and anti-phase oscillations of the two output currents as well as a smooth phase shift when sweeping a side gate have been reproduced. By injecting an electron into the upper rail $|0\rangle$, the wave function will evolve into a superposition of symmetric and anti-symmetric states. While travelling through the interaction region, the wave function of the electron will then pick up a phase and will evolve into a superposition of $|0\rangle$ and $|1\rangle$ [7] as shown in Fig. 12 by a simulation example.

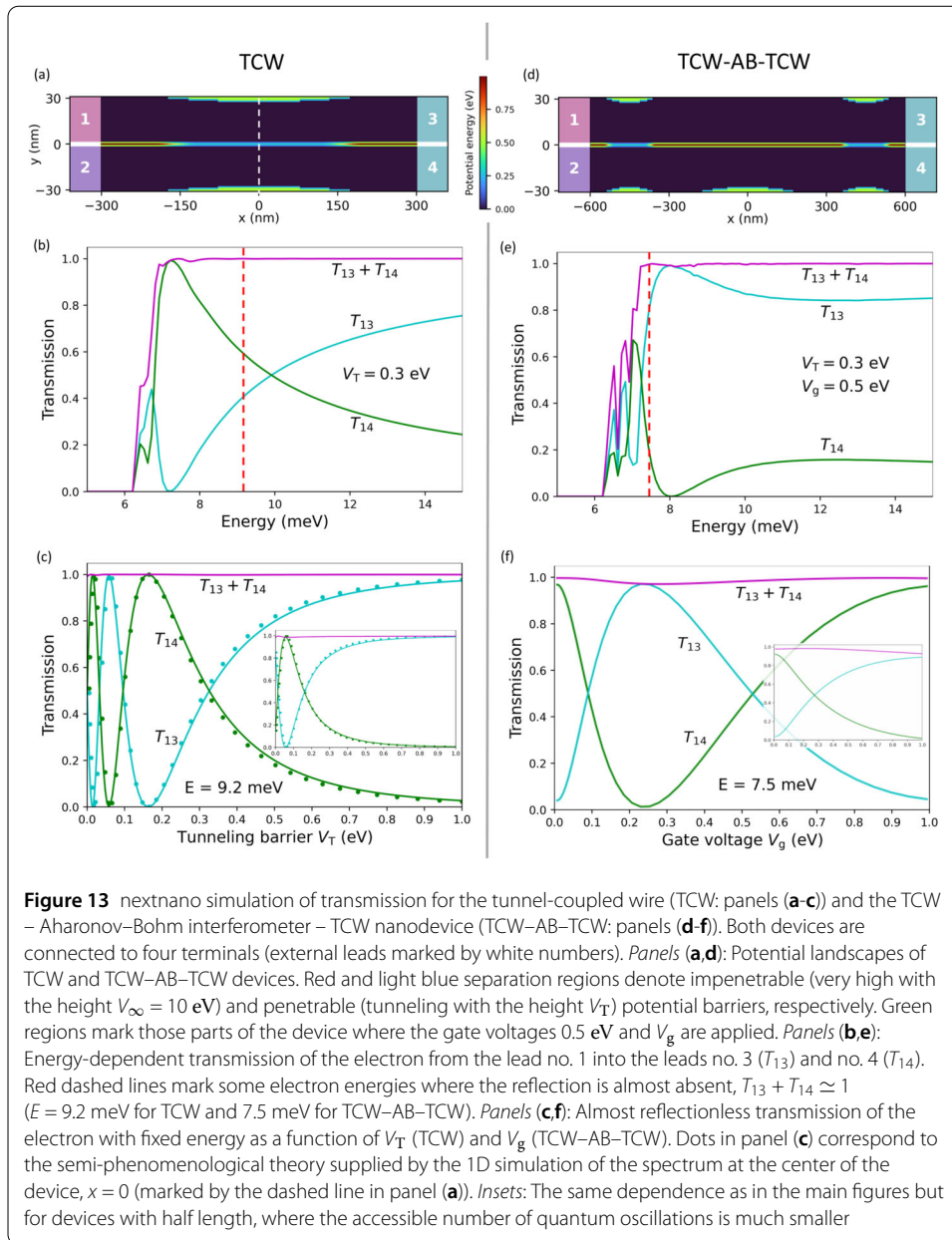
Simulations of pLDoS and transmission through nanodevices: Eq. (1) describes how the ideal electron flying qubit is expected to operate: The electron is injected in either the upper or lower incoming channel (see Fig. 1b) and propagates without reflection through the quantum device, where the electron state is rotated in the Hilbert space. This rotation can be illustrated with the help of the Bloch sphere, Fig. 1a. Angles θ and ϕ are generated by the tunneling regions and interferometers, respectively. The output state is a coherent



superposition of the states $|0\rangle$ and $|1\rangle$. It is controlled by the tunneling barriers and either by the magnetic field or by the asymmetric bias of the interferometer. Since using the magnetic field is technologically inconvenient, we focus in this section on the asymmetrically biased interferometers.

There are two points which have fundamental importance for engineering the electron flying qubits. Namely, one needs an experimental setup where, on one hand, the reflection is reduced to a minimum and, on the other hand, the sensitivity of the electron state to the respective gate voltages is high. Let us explain how using the nextnano software helps to find such a setup.

To this end, nextnano enables the calculation of the pLDoS and the transmission of the nanodevices using the CBR method [149, 153]. In the following, we demonstrate such calculation via two cases that are the central building blocks of the electron-flying-qubit architecture. Firstly (see left columns of Fig. 12 and Fig. 13), we address electron propagation through a tunnel-coupled wire (TCW). We remind readers that here at $y = 0$ a narrow potential barrier is present between two transport channels that allows for coherent tunneling of the electron. Secondly (see right columns of Fig. 12 and Fig. 13), we



investigate electron propagation through a quantum interferometer (compare Fig. 1b,d) where two TCWs embrace an AB island enabling full control of the quantum state via magnetic and geometric phase manipulations. The potential profile of both models is shown in Fig. 13a,d. For such study of a nanoscale device, materials properties have to be specified in the nextnano input file such that the potential energies are properly set. We have used GaAs for the device and leads, and adjusted the potential energy in different regions representing high insulating barriers (red lines), tunneling barriers (light blue lines), and gates (green regions). The potential energy at the gates can be tuned by applying gate voltages and the strengths of the barriers are given in Fig. 13 and its caption.

Several examples of the pLDoS are shown in Fig. 12 which have been generated using the nextnano software. In these simulations, the electron has been injected into lead no. 1

with a given energy that is $E = 9.2$ meV for TCW and $E = 7.5$ meV for the quantum interferometer (TCW–AB–TCW). Slices of the pLDoS are shown at these energies.

Let us first discuss the TCW (left column of Fig. 12) for different voltages (V_T) applied on the tunnel-barrier gate. The TCW is able to change only the angle θ – see Eq. (1). Thus, the output state can be written as $|\Psi\rangle_{\text{TCW}} \propto \cos(\theta/2)|0\rangle + \sin(\theta/2)|1\rangle$. When the tunneling barrier is absent (Fig. 13a), one observes at the output an equal superposition of $|0\rangle$ and $|1\rangle$ which can occur at either $\theta = \pi/2$ or $\theta = 3\pi/2$, both corresponding to two points on the equator of the Bloch sphere (Fig. 1). Since a small increase of V_T drives the output state to $|0\rangle$ (Fig. 13b) corresponding to the north pole of the Bloch sphere, we conclude that in barrier-less setup $\theta = 3\pi/2$. With further increasing V_T , the output state becomes $|1\rangle$, i.e. the south pole of the Bloch sphere (Fig. 13c, $\theta = \pi$) and returns to the equator (Fig. 13d, $\theta = \pi/2$). The latter point is the opposite equator point to that of the barrier-less setup. When the tunneling barrier becomes high (Fig. 12d) one enters the regime of two fully decoupled transport channels with output state $|0\rangle$. Clearly, these coherent tunnel oscillations of the electron wave function manifest themselves in the quantum oscillations of the transmission via a TCW (see Fig. 13c).

Secondly, let us focus on electron propagation through the quantum interferometer (Fig. 12f–j). Increasing the potential on a side gate of the lower transport channel (V_g) modifies the geometric phase of the electron's quantum state and changes the second angle ϕ in Eq. (1). This, in turn, causes coherent oscillations between the output terminals 3 and 4, i.e. oscillations between output states $|0\rangle$ and $|1\rangle$, and results in quantum oscillations of the TCW–AB–TCW transmission (see Fig. 13f). The tunnel regions in the example of Figs. 12f–j are the same and each of them changes the angle θ by $\pi/2$. This is apparent from Fig. 12a where $V_g = 0$ and $\phi = 0$: the output state after successive rotation in two TCW regions is $|1\rangle$, i.e. the total change of θ in the TCWs is π . Therefore, each individual connection changes θ by $\pi/2$. This allows one to approximate the output state as $|\Psi\rangle_{\text{TCW–AB–TCW}} \propto (e^{i\phi} - 1)|0\rangle + (e^{i\phi} + 1)|1\rangle$ [7]. Similar to the analysis of the pLDoS in the TCW, we can now trace rotations of the electron state with increasing V_g . Two output states shown in Fig. 12g,i correspond to two opposite points on the equator of the Bloch sphere with $\phi = \pi/2$ and $\phi = 3\pi/2$. The south pole of the Bloch sphere is reached in Fig. 12j despite a substantial blockage of the lower transport path by the strong gate potential of the side gate.

To conclude the discussion of the pLDoS, we note that a detailed analysis of the flying qubit geometry in relation with experiments has also been performed using a combination of the theoretical approach and the KWANT software, see Ref. [145].

Having discussed electron propagation at a qualitative level via the pLDoS, let us now investigate electron propagation in a more quantitative way employing energy dependent transmission, $T_{ij}(E)$ from the first lead to the output leads no. 3 and no. 4. First, we study the dependence on the injection energy (Fig. 13b,e). The energy of the incoming electron is counted from the potential energy of the lead no. 1. All device parameters are fixed at this stage. Transmission is zero if the electron energy is smaller than the energy of propagating states of the device, that is below 6.2 meV for the chosen parameters. Above this threshold, transmission starts to grow. However, it is first accompanied by substantial reflection of the electron to the input leads no. 1 and no. 2 which are described by T_{11} and T_{12} (not shown). This is apparent in the central panels of Fig. 13, up to an energy of about 7 meV, where the total transmission, $T_{\text{total}} = T_{13} + T_{14}$ (magenta lines), is smaller than the ideal

value, $T_{\text{total}} < T_{\text{ideal}} = 1$. In a second step, we have identified the energy at which $T_{\text{total}} \simeq 1$ (i.e. reflection is minimised) but $T_{13}, T_{14} \neq 0, 1$. In this regime, we expect strong sensitivity of the electron state $|\psi\rangle$, Eq. (1), to the gates and the barriers of the quantum device. Two examples of these energies are shown by red dashed vertical lines and are studied at the second stage of the simulations. Fixing these two energies for the TCW and the quantum interferometer, we have studied the dependence of the transmission on the potential of the tunnel barrier, V_T (Fig. 13c), and the side gate, V_g (Fig. 13f). The goal of this stage is twofold: We identify regions of the parameters where T_{total} (magenta lines) is close to the ideal value of 1 and, simultaneously, the rotation of the electron states is pronounced. The latter condition is fulfilled by the crossover between regimes $T_{13} < T_{14}$ and $T_{13} > T_{14}$. The vicinity of the crossover can be chosen as an operation range of the qubit (or of the qubit element), provided the reflection is almost absent. In order to find optimal parameters which provide both ideal transmission and range for manipulation of the quantum phase, simulations such as the here-discussed case are helpful to identify experimentally relevant voltage ranges. The here-discussed simulations indicate that sufficient control is obtained in TCW and AB regions with the length ≥ 500 nm and further allow to identify optimal operation voltages. Let us discuss these aspects in more detail for the TCW and the quantum interferometer.

TCW: A simple phenomenological scattering theory predicts that $T_{13} \simeq \cos^2(\delta\phi_{\text{TCW}}/2)$, $T_{14} \simeq \sin^2(\delta\phi_{\text{TCW}}/2)$, $\delta\phi_{\text{TCW}} \equiv \delta k L_{\text{TCW}}$, where $\delta k = k_1 - k_2$ is the difference of wave vectors of two modes with the lowest energy, which support the transmission, and L_{TCW} is the effective spatial scale of the region, where the tunneling takes place [7]. The quantum phase $\delta\phi_{\text{TCW}}$ is expected to grow with increasing the length of the tunneling barrier, L_{tun} , which is equal to 300 nm in the example of the left column of Fig. 13. We distinguish L_{TCW} and L_{tun} since the former depends on the shape of the electrostatic potential inside the device. Therefore, one may expect $L_{\text{TCW}} \ll L_{\text{tun}}$. This inequality has been confirmed by a comparison of the scattering theory (green and cyan dots in Fig. 13c) with the outcome of the true 2D simulations (solid lines in the same figure). L_{TCW} is the only adjustable parameter of this comparison. The value of δk has been found by using the dispersion relation of almost free electrons propagating in a semiconductor, $E_{1,2} = (\hbar k_{1,2})^2/2m^*$. Energy levels $E_{1,2}$ have been obtained from 1D simulations of the spectrum at the 1D transverse cross section in the center of the device (dashed line in Fig. 13a). Interestingly, the ratio $L_{\text{TCW}}/L_{\text{tun}}$ is almost insensitive to the transverse size of the device. An excellent agreement between the 2D simulations and the scattering theory suggests that the latter can be used as a compact model of TCW in simulations of more complicated circuits. Such a simplification will allow one to minimize computer resources needed for the simulations. The inset in Fig. 13c shows that the range of V_T , where the quantum oscillations occur, shrinks with making L_{tun} , and correspondingly the space for the quantum interference, smaller. Since T_{total} is very close to 1 (no reflection) in the entire range $0 < V_T < 1$ eV, such an idealized qubit would operate properly in a vicinity of any crossover point where $T_{13} \simeq T_{14}$, e.g. $V_T \sim 0.1$ eV or $V_T \sim 0.33$ eV.

Interferometer: When the electron modes propagate through the upper and lower arms of the electrostatic version of the Aharonov–Bohm interferometer, they acquire a relative phase which governs the quantum interference. If the interferometer is connected directly to the leads, the transmission through the device can be estimated as $\mathcal{T}_{\text{AB}} = \cos^2(e\delta V \tau_{\text{AB}}/2\hbar)$ [165]. Here, τ_{AB} is the flight time of the electron through the unit. In

the ballistic case, it is the ratio of the interferometer length over the electron velocity, $\tau_{AB} = L_{AB}/v$. We have introduced the relative total potential, $\delta V = V_u - V_l$ (integrated over the upper, V_u , or lower, V_l , arm), which the electron feels inside the interferometer. The interference oscillations are more pronounced in longer devices, compare results presented in Fig. 13f and its inset. To avoid complexity, we do not discuss here semi-phenomenological analytical calculation of transmission for the composite TCW–AB–TCW device and do not compare the scattering theory with the 2D simulations. Similar to the TCW device, it is useful to tune V_g to the vicinity of the crossover point where $T_{13} \simeq T_{14}$, i.e. either $V_g \sim 0.1$ eV or $V_g \sim 0.5$ eV in the example of Fig. 13f. Note, however, that $T_{\text{total}} < 1$ in both cases. Clearly, the preference should be given to the regime with smaller reflection, i.e. the second crossover point in the simulated example.

The above predictions of numerical simulations serve as important input for experimental realisations of the flying qubit. Integrating the simulation additionally in a feedback loop of the workflow (Fig. 9) would enable to find optimised device geometries tailored to the different approaches such as Levitons or SAW. To conclude this section, we would like to mention that the applications of the nextnano software can be very broad since it can straightforwardly be adapted for modelling devices made from other semiconductor materials (e.g., industrially highly relevant SiGe), for including effects of the magnetic field on the interferometer, for mimicking dephasing and decoherence with the help of the artificially connected leads, to name just a few.

3.2 Low energy time-resolved and many-body simulations

In the previous section, we have focused on the simulation of the static properties of the devices. Solving the corresponding quantum-electrostatic problem allows one to understand how macroscopic parameters, usually the geometry of the electrostatic gates that are set to typical values of order ≤ 1 eV, influence the active quantum part of the device where the relevant energies are in the meV range. Once this is understood, the next step is to simulate actual time-resolved experiments that involve sub-meV physics (typical time in the 1–100 ps range). The goal is to understand the propagation of pulses, the coupling between different pulses (at the origin of the two-flying-qubits gates), the renormalisation of the velocity due to Coulomb interactions [53] and other effects such as different decoherence and relaxation channels. These theoretical developments are very much on-going research for which no standard approaches have yet emerged. As in-depth discussion of these aspects goes beyond the scope of the present review, we refer to Ref. [7] for pointers to the literature or to Ref. [166] for an introduction to the non-interacting formalism and to Ref. [144] for illustrative time-dependent simulations of the propagation of voltage pulses, in particular in the quantum Hall regime [167].

These methods have not been included into the nextnano software, however, TKWANT, the time-dependent extension of the KWANT software is able to provide an appropriate platform which is complementary to the nextnano one. Both KWANT and TKWANT software packages are distributed under the BSD license which imposes minimal restrictions on the use and distribution of this software. Consequently, algorithms developed by the KWANT team could be incorporated into commercial software packages targeting specific quantum industry applications, such as electron-flying-qubit devices. The principal developers of KWANT are from CEA Grenoble and TU Delft.

Note that there are no general purpose simulation approaches that can handle many-body problems in an exact and systematic way except in very particular cases. Most approaches rely on some approximation scheme whose validity must be checked a posteriori. A promising route followed by some of us to design a systematic method with a controlled accuracy uses calculations of high order processes (i.e. processes where electrons interact strongly) made possible by the use of a machine learning approach to evaluate the corresponding high dimensional integrals [168].

4 Conclusion and outlook

The realisation of flying qubits with single electrons opens a novel, viable route of quantum technology with considerable potential for quantum-computation applications. In this review we introduced the novel electron-flying-qubit approach and discussed three equally promising transport techniques – surface acoustic waves (SAW), hot-electron emission from quantum-dot pumps and Levitons – which are rapidly advancing. Owing to similarities between the different approaches – such as emission from a gate-defined quantum dot in SAW-transport and the electron pump – we suspect that progress in one-field will also drive the others. Based on latest progress and relevant simulation cases, we showed that numerical modelling of quantum devices is decisive to speed up experimental deployment cycles towards the first implementation of an electron flying qubit. We anticipate that automatised optimisation of the device design via numerical modelling will enable nanofabrication tailored for efficient quantum operations.

In order to make the electron flying qubit competitive with cutting-edge approaches in the field of quantum computation, it is of central importance to develop ultrafast real-time control of quantum operations. An appealing approach to implement such in-flight quantum operations is to use ultrafast voltage pulses in the picosecond range and below. On-chip optoelectronic conversion of a femtosecond laser pulse is so far the most promising technique to generate electrical pulses on the picosecond scale [116–118]. Combined with recent conversion efficiency improvements of these optoelectronic devices [119, 120, 169, 170], such a real-time control is in reach and is currently pursued in the *UltraFastNano* project. Using these techniques, single-electron wave packets with a temporal width of 1 ps can be generated. The thus-enabled miniaturisation of quantum interferometers will allow the implementation of hundreds of quantum operations within the coherence time. Furthermore, ultrafast gate control will provide a possibility to resolve quantum states in real time. Rather than measuring the coherent oscillations of the electron qubits by varying the strength of the tunnel coupling [42], one can simply control the tunnel barrier in a time-resolved manner. This enables to keep the electrostatic confinement potential of the entire device constant and only vary the tunnel barrier on the time scale needed for the quantum operation.

The progress in the field strongly depends on the availability of tools for the reliable modelling of the quantum devices. The simulations must possess enough predictive power to suggest the most suitable device geometry prior to the fabrication of the device in a clean room. Iterations and tests of the devices are costly and time consuming and should be reduced to the strict minimum with the help of the high-precision professional simulations. Adding more and more qubits into quantum circuits will increase drastically the experimental parameter space for device tuning. Therefore, automatic tuning of all the gate voltages by using concepts from artificial intelligence and machine-learning would

have to be implemented in platforms for the theoretical modelling. We anticipate that the synergy of semiconductor quantum technology with cutting-edge numerical simulations paves the way for electron-flying-qubit implementations fostering the industrial applicability of quantum computation.

Acknowledgements

CB acknowledges helpful discussions with J.-M. Gérard.

Funding

We acknowledge funding from the European Union's Horizon 2020 research and innovation programme under grant agreement No. 862683 (UltraFastNano). EC acknowledges funding from the European Union's Horizon 2020 research and innovation programme under the Marie Skłodowska-Curie grant agreement No. 840550 (PRESQUE). JW acknowledges funding from the European Union's Horizon 2020 research and innovation programme under the Marie Skłodowska-Curie grant agreement No. 754303 (GreQuE). CB, DCG and XW acknowledge funding from the French National Funding Agency (ANR) through project ANR-16-CE30-0015-02 (FullyQuantum). CB and GG acknowledge funding from the French National Funding Agency (ANR) through project ANR-19-CE47-0005 (STEPforQUBITS).

Availability of data and materials

Numerical codes and tutorials can be found at <https://kwant-project.org> and <https://www.nextnano.com>.

Declarations

Competing interests

The authors declare that they have no competing interests.

Author contribution

HE, JW, EC, MCdSF, MK, JS, XW, DCG, SB, AT, TG, OY and CB wrote the article with input from all authors. TC, GG and SO contributed to the device fabrication. PP contributed to the experimental set-up. HE, JW, EC, MCdSF, CG, AL, PR, KÖ, MA prepared the figures. All authors read and approved the final manuscript.

Author details

¹Univ. Grenoble Alpes, CNRS, Grenoble INP, Institut Néel, 25 rue des Martyrs, 38000 Grenoble, France. ²PHELIQS, Université Grenoble Alpes, CEA, Grenoble INP, IRIG, Grenoble 38000, France. ³James Watt School of Engineering, Electronics and Nanoscale Engineering, University of Glasgow, University Avenue, Glasgow G12 8QQ, United Kingdom. ⁴SPEC, Université Paris-Saclay, CEA, CNRS, Gif sur Yvette 91191, France. ⁵National Physical Laboratory, Hampton Road, Teddington, Middlesex TW11 0LW, United Kingdom. ⁶Department of Microtechnology and Nanoscience (MC2), Chalmers University of Technology, Göteborg, S-412 96, Sweden. ⁷nextnano GmbH, Konrad-Zuse-Platz 8, 81829 München, Germany. ⁸nextnano Lab, 12 chemin des prunelles, 38700 Corenc, France.

Publisher's Note

Springer Nature remains neutral with regard to jurisdictional claims in published maps and institutional affiliations.

Received: 3 September 2021 Accepted: 12 July 2022 Published online: 10 August 2022

References

1. DiVincenzo DP. The physical implementation of quantum computation. *Fortschr Phys.* 2000;48(9–11):771–83. [https://doi.org/10.1002/1521-3978\(200009\)48:9<771::AID-PROP771>3.0.CO;2-E](https://doi.org/10.1002/1521-3978(200009)48:9<771::AID-PROP771>3.0.CO;2-E).
2. Wehner S, Elkouss D, Hanson R. Quantum Internet: a vision for the road ahead. *Science.* 2018;362(6412):9288. <https://doi.org/10.1126/science.aam9288>.
3. Peruzzo A, McClean J, Shadbolt P, Yung M-H, Zhou X-Q, Love PJ, Aspuru-Guzik A, O'Brien JL. A variational eigenvalue solver on a photonic quantum processor. *Nat Commun.* 2014;5(1):4213. <https://doi.org/10.1038/ncomms5213>.
4. Knill E, Laflamme R, Milburn GJ. A scheme for efficient quantum computation with linear optics. *Nature.* 2001;409(6816):46–52. <https://doi.org/10.1038/35051009>.
5. Kok P, Munro WJ, Nemoto K, Ralph TC, Dowling JP, Milburn GJ. Linear optical quantum computing with photonic qubits. *Rev Mod Phys.* 2007;79:135–74. <https://doi.org/10.1103/RevModPhys.79.135>.
6. Lodahl P. Quantum-dot based photonic quantum networks. *Quantum Sci Technol.* 2018;3(1):013001. <https://doi.org/10.1088/2058-9565/aa91bb>.
7. Bäuerle C, Glattli DC, Meunier T, Portier F, Roche P, Roulleau P, Takada S, Waintal X. Coherent control of single electrons: a review of current progress. *Rep Prog Phys.* 2018;81(5):056503. <https://doi.org/10.1088/1361-6633/aaa98a>.
8. Clauser JF. Experimental distinction between the quantum and classical field-theoretic predictions for the photoelectric effect. *Phys Rev D.* 1974;9:853–60. <https://doi.org/10.1103/PhysRevD.9.853>.
9. Eisaman MD, Fan J, Migdall A, Polyakov SV. Invited review article: single-photon sources and detectors. *Rev Sci Instrum.* 2011;82(7):071101. <https://doi.org/10.1063/1.3610677>.
10. Michler P, Kiraz A, Becher C, Schoenfeld WV, Petroff PM, Zhang L, Hu E, Imamoglu A. A quantum dot single-photon turnstile device. *Science.* 2000;290(5500):2282–5. <https://doi.org/10.1126/science.290.5500.2282>.

11. Senellart P, Solomon G, White A. High-performance semiconductor quantum-dot single-photon sources. *Nat Nanotechnol.* 2017;12(11):1026–39. <https://doi.org/10.1038/nnano.2017.218>.
12. Arcari M, Söllner I, Javadi A, Lindskov Hansen S, Mahmoodian S, Liu J, Thyrrestrup H, Lee EH, Song JD, Stobbe S, Lodahl P. Near-unity coupling efficiency of a quantum emitter to a photonic crystal waveguide. *Phys Rev Lett.* 2014;113:093603. <https://doi.org/10.1103/PhysRevLett.113.093603>.
13. Uppu R, Pedersen FT, Wang Y, Olesen CT, Papon C, Zhou X, Midolo L, Scholz S, Wieck AD, Ludwig A, Lodahl P. Scalable integrated single-photon source. *Sci Adv.* 2020;6(50). <https://doi.org/10.1126/sciadv.abc8268>.
14. Santori C, Fattal D, Vučković J, Solomon GS, Yamamoto Y. Indistinguishable photons from a single-photon device. *Nature.* 2002;419(6907):594–7. <https://doi.org/10.1038/nature01086>.
15. He Y-M, He Y, Wei Y-J, Wu D, Atatüre M, Schneider C, Höfling S, Kamp M, Lu C-Y, Pan J-W. On-demand semiconductor single-photon source with near-unity indistinguishability. *Nat Nanotechnol.* 2013;8(3):213–7. <https://doi.org/10.1038/nnano.2012.262>.
16. Munsch M, Malik NS, Dupuy E, Delga A, Bleuse J, Gérard J-M, Claudon J, Gregersen N, Mørk J. Dielectric GaAs antenna ensuring an efficient broadband coupling between an InAs quantum dot and a Gaussian optical beam. *Phys Rev Lett.* 2013;110:177402. <https://doi.org/10.1103/PhysRevLett.110.177402>.
17. Somaschi N, Giesz V, De Santis L, Loredò J, Almeida MP, Hornecker G, Portalupi SL, Grange T, Anton C, Demory J, Gómez C, Sagnes I, Lanzillotti-Kimura ND, Lemaître A, Auffèves A, White AG, Lanco L, Senellart P. Near-optimal single-photon sources in the solid state. *Nat Photonics.* 2016;10(5):340–5. <https://doi.org/10.1038/nphoton.2016.23>.
18. Tomm N, Javadi A, Antoniadis NO, Najer D, Löbl MC, Korsch AR, Schott R, Valentin SR, Wieck AD, Ludwig A, Warburton RJ. A bright and fast source of coherent single photons. *Nat Nanotechnol.* 2021;16(4):399–403. <https://doi.org/10.1038/s41565-020-00831-x>.
19. Lesovik GB. Excess quantum noise in 2D ballistic point contacts. *JETP Lett.* 1989;49:592–4.
20. Büttiker M. Scattering theory of current and intensity noise correlations in conductors and wave guides. *Phys Rev B.* 1992;46:12485–507. <https://doi.org/10.1103/PhysRevB.46.12485>.
21. Landauer R, Martin T. Equilibrium and shot noise in mesoscopic systems. *Physica B.* 1991;175:167–77. [https://doi.org/10.1016/0921-4526\(91\)90710-V](https://doi.org/10.1016/0921-4526(91)90710-V).
22. Henny M, Oberholzer S, Strunk C, Heinzel T, Ensslin K, Holland M, Schönenberger C. The fermionic Hanbury Brown and Twiss experiment. *Science.* 1999;284(5412):296–8. <https://doi.org/10.1126/science.284.5412.296>.
23. Oliver WD, Kim J, Liu RC, Yamamoto Y. Hanbury Brown and Twiss-type experiment with electrons. *Science.* 1999;284(5412):299–301. <https://doi.org/10.1126/science.284.5412.299>.
24. Liu RC, Odom B, Yamamoto Y, Tarucha S. Quantum interference in electron collision. *Nature.* 1998;391:263.
25. Ji Y, Chung Y, Sprinzak D, Heiblum M, Mahalu D, Shtrikman H. An electronic Mach–Zehnder interferometer. *Nature.* 2003;422(6930):415–8. <https://doi.org/10.1038/nature01503>.
26. Fève G, Mahé A, Berroir J-M, Kontos T, Plaças B, Glattli DC, Cavanna A, Etienne B, Jin Y. An on-demand coherent single-electron source. *Science.* 2007;316(5828):1169–72. <https://doi.org/10.1126/science.1141243>.
27. Blumenthal MD, Kaestner B, Li L, Giblin S, Janssen TJBM, Pepper M, Anderson D, Jones G, Ritchie DA. Gigahertz quantized charge pumping. *Nat Phys.* 2007;3:343.
28. Hermelin S, Takada S, Yamamoto M, Tarucha S, Wieck AD, Saminadayar L, Bäuerle C, Meunier T. Electrons surfing on a sound wave as a platform for quantum optics with flying electrons. *Nature.* 2011;477:435.
29. McNeil RPG, Kataoka M, Ford CJB, Barnes CHW, Anderson D, Jones GAC, Farrer I, Ritchie DA. On-demand single-electron transfer between distant quantum dots. *Nature.* 2011;477:439.
30. Dubois J, Jullien T, Portier F, Roche P, Cavanna A, Jin Y, Wegscheider W, Rouleau P, Glattli DC. Minimal-excitation states for electron quantum optics using levitons. *Nature.* 2013;502:659. <https://doi.org/10.1038/nature12713>.
31. Takada S, Edlbauer H, Lepage HV, Wang J, Mortemousque P-A, Georgiou G, Barnes CHW, Ford CJB, Yuan M, Santos PV, Waintal X, Ludwig A, Wieck AD, Urdampilleta M, Meunier T, Bäuerle C. Sound-driven single-electron transfer in a circuit of coupled quantum rails. *Nat Commun.* 2019;10:4557. <https://doi.org/10.1038/s41467-019-12514-w>.
32. Freise L, Gerster T, Reifert D, Weimann T, Pierz K, Hohls F, Ubbelohde N. Trapping and counting ballistic nonequilibrium electrons. *Phys Rev Lett.* 2020;124(12):127701. <https://doi.org/10.1103/PhysRevLett.124.127701>.
33. Giblin SP, Kataoka M, Fletcher JD, See P, Janssen TJBM, Griffiths JP, Jones GAC, Farrer I, Ritchie DA. Towards a quantum representation of the ampere using single electron pumps. *Nat Commun.* 2012;3:930.
34. Stein F, Scherer H, Gerster T, Behr R, Gotz M, Pesel E, Leicht C, Ubbelohde N, Weimann T, Pierz K, Schumacher HW, Hohls F. Robustness of single-electron pumps at sub-ppm current accuracy level. *Metrologia.* 2017;54(1):1. <https://doi.org/10.1088/1681-7575/54/1/S1>.
35. Moreau E, Robert I, Gérard JM, Abram I, Manin L, Thierry-Mieg V. Single-mode solid-state single photon source based on isolated quantum dots in pillar microcavities. *Appl Phys Lett.* 2001;79(18):2865–7. <https://doi.org/10.1063/1.1415346>.
36. Thomas S, Senellart P. The race for the ideal single-photon source is on. *Nat Nanotechnol.* 2021;16(4):367–8. <https://doi.org/10.1038/s41565-021-00851-1>.
37. Hayashi T, Fujisawa T, Cheong HD, Jeong YH, Hirayama Y. Coherent manipulation of electronic states in a double quantum dot. *Phys Rev Lett.* 2003;91:226804. <https://doi.org/10.1103/PhysRevLett.91.226804>.
38. Petta JR, Johnson AC, Marcus CM, Hanson MP, Gossard AC. Manipulation of a single charge in a double quantum dot. *Phys Rev Lett.* 2004;93:186802. <https://doi.org/10.1103/PhysRevLett.93.186802>.
39. Petersson KD, Petta JR, Lu H, Gossard AC. Quantum coherence in a one-electron semiconductor charge qubit. *Phys Rev Lett.* 2010;105:246804. <https://doi.org/10.1103/PhysRevLett.105.246804>.
40. Stockklauser A, Scarlino P, Koski JV, Gasparinetti S, Andersen CK, Reichl C, Wegscheider W, Ihn T, Ensslin K, Wallraff A. Strong coupling cavity QED with gate-defined double quantum dots enabled by a high impedance resonator. *Phys Rev X.* 2017;7:011030. <https://doi.org/10.1103/PhysRevX.7.011030>.
41. Rouleau P, Portier F, Roche P, Cavanna A, Faini G, Gennser U, Mailly D. Direct measurement of the coherence length of edge states in the integer quantum Hall regime. *Phys Rev Lett.* 2008;100:126802. <https://doi.org/10.1103/PhysRevLett.100.126802>.
42. Yamamoto M, Takada S, Bäuerle C, Watanabe K, Wieck AD, Tarucha S. Electrical control of a solid-state flying qubit. *Nat Nanotechnol.* 2012;7:247–51. <https://doi.org/10.1038/nnano.2012.28>.

43. Duprez H, Sivre E, Anthore A, Aassime A, Cavanna A, Querghi A, Gennser U, Pierre F. Macroscopic electron quantum coherence in a solid-state circuit. *Phys Rev X*. 2019;9:021030. <https://doi.org/10.1103/PhysRevX.9.021030>.
44. Duprez H, Sivre E, Anthore A, Aassime A, Cavanna A, Gennser U, Pierre F. Transmitting the quantum state of electrons across a metallic island with Coulomb interaction. *Science*. 2019;366(6470):1243–7. <https://doi.org/10.1126/science.aaw7856>.
45. Ladd TD, Jelezko F, Laflamme R, Nakamura Y, Monroe C, O'Brien JL. Quantum computers. *Nature*. 2010;464:45–53. <https://doi.org/10.1038/nature08812>.
46. Popkin G. Scientists are close to building a quantum computer that can beat a conventional one. *Science*. 2016. <https://doi.org/10.1126/science.aal0442>.
47. Kjaergaard M, Schwartz ME, Braumüller J, Krantz P, Wang JI-J, Gustavsson S, Oliver WD. Superconducting qubits: current state of play. *Annu Rev Condens Matter Phys*. 2020;11(1):369–95. <https://doi.org/10.1146/annurev-conmatphys-031119-050605>.
48. Bruzewicz CD, Chiaverini J, McConnell R, Sage JM. Trapped-ion quantum computing: progress and challenges. *Appl Phys Rev*. 2019;6(2):021314. <https://doi.org/10.1063/1.5088164>.
49. Stano P, Loss D. Review of performance metrics of spin qubits in gated semiconducting nanostructures. 2021. [arXiv:2107.06485](https://arxiv.org/abs/2107.06485).
50. UltraFastNano. Electronic generation and detection in nanoelectronic devices at the picosecond scale. 2020. <https://cordis.europa.eu/project/id/862683>.
51. Niimi Y, Baines Y, Capron T, Maillly D, Lo F-Y, Wieck AD, Meunier T, Saminadayar L, Bäuerle C. Effect of disorder on the quantum coherence in mesoscopic wires. *Phys Rev Lett*. 2009;102:226801. <https://doi.org/10.1103/PhysRevLett.102.226801>.
52. Niimi Y, Baines Y, Capron T, Maillly D, Lo F-Y, Wieck AD, Meunier T, Saminadayar L, Bäuerle C. Quantum coherence at low temperatures in mesoscopic systems: effect of disorder. *Phys Rev B*. 2010;81:245306. <https://doi.org/10.1103/PhysRevB.81.245306>.
53. Roussely G, Arrighi E, Georgiou G, Takada S, Schalk M, Urdampilleta M, Ludwig A, Wieck AD, Armagnat P, Kloss T, Waintal X, Meunier T, Bäuerle C. Unveiling the bosonic nature of an ultrashort few-electron pulse. *Nat Commun*. 2018;9:2811. <https://doi.org/10.1038/s41467-018-05203-7>.
54. Bocquillon E, Freulon V, Berroir J-M, Degiovanni P, Plaças B, Cavanna A, Jin Y, Fève G. Coherence and indistinguishability of single electrons emitted by independent sources. *Science*. 2013;339(6123):1054–7. <https://doi.org/10.1126/science.1232572>.
55. Thomas C, Hatke AT, Tuaz A, Kallaher R, Wu T, Wang T, Diaz RE, Gardner GC, Capano MA, Manfra MJ. High-mobility InAs 2DEGs on GaSb substrates: a platform for mesoscopic quantum transport. *Phys Rev Materials*. 2018;2:104602. <https://doi.org/10.1103/PhysRevMaterials.2.104602>.
56. Chung YJ, Villegas Rosales KA, Baldwin KW, Madathil PT, West KW, Shayegan M, Pfeiffer LN. Ultra-high-quality two-dimensional electron systems. *Nat Mater*. 2021;20(5):632–7. <https://doi.org/10.1038/s41563-021-00942-3>.
57. Talyanskii VI, Shilton JM, Pepper M, Smith CG, FordCJB, Linfield EH, Ritchie DA, Jones GAC. Single-electron transport in a one-dimensional channel by high-frequency surface acoustic waves. *Phys Rev B*. 1997;56:15180–4. <https://doi.org/10.1103/PhysRevB.56.15180>.
58. Kaestner B, Kashcheyevs V, Amakawa S, Blumenthal MD, Li L, Janssen TJB, Hein G, Pierz K, Weimann T, Siegner U, Schumacher HW. Single-parameter nonadiabatic quantized charge pumping. *Phys Rev B*. 2008;77:153301. <https://doi.org/10.1103/PhysRevB.77.153301>.
59. Yamahata G, Giblin SP, Kataoka M, Karasawa T, Fujiwara A. High-accuracy current generation in the nanoampere regime from a silicon single-trap electron pump. *Sci Rep*. 2017;7(1):45137. <https://doi.org/10.1038/srep45137>.
60. Kaestner B, Kashcheyevs V. Non-adiabatic quantized charge pumping with tunable-barrier quantum dots: a review of current progress. *Rep Prog Phys*. 2015;78(10):103901. <https://doi.org/10.1088/0034-4885/78/10/103901>.
61. Jullien T, Roulleau P, Roche B, Cavanna A, Jin Y, Glatli DC. Quantum tomography of an electron. *Nature*. 2014;514:603.
62. Bisognin R, Marguerite A, Roussel B, Kumar M, Cabart C, Chapdelaine C, Mohammad-Djafari A, Berroir J-M, Bocquillon E, Plaças B, Cavanna A, Gennser U, Jin Y, Degiovanni P, Fève G. Quantum tomography of electrical currents. *Nat Commun*. 2019;10:3379. <https://doi.org/10.1038/s41467-019-11369-5>.
63. Wixforth A, Kotthaus JP, Weimann G. Quantum oscillations in the surface-acoustic-wave attenuation caused by a two-dimensional electron system. *Phys Rev Lett*. 1986;56:2104–6. <https://doi.org/10.1103/PhysRevLett.56.2104>.
64. Morgan D. Surface acoustic wave filters: with applications to electronic communications and signal processing. 2nd ed. Oxford: Academic Press; 2007.
65. de Lima MM, Santos PV. Modulation of photonic structures by surface acoustic waves. *Rep Prog Phys*. 2005;68(7):1639–701. <https://doi.org/10.1088/0034-4885/68/7/r02>.
66. Kataoka M, Astley MR, Thorn AL, Oi DKL, Barnes CHW, Ford CJB, Anderson D, Jones GAC, Farrer I, Ritchie DA, Pepper M. Coherent time evolution of a single-electron wave function. *Phys Rev Lett*. 2009;102:156801. <https://doi.org/10.1103/PhysRevLett.102.156801>.
67. Ito R, Takada S, Ludwig A, Wieck AD, Tarucha S, Yamamoto M. Coherent beam splitting of flying electrons driven by a surface acoustic wave. *Phys Rev Lett*. 2021;126:070501. <https://doi.org/10.1103/PhysRevLett.126.070501>.
68. Edlbauer H, Wang J, Ota S, Richard A, Jadot B, Mortemousque P-A, Okazaki Y, Nakamura S, Koderia T, Kaneko N-H, Ludwig A, Wieck AD, Urdampilleta M, Meunier T, Bäuerle C, Takada S. In-flight distribution of an electron within a surface acoustic wave. *Appl Phys Lett*. 2021;119(11):114004. <https://doi.org/10.1063/5.0062491>.
69. Jadot B, Mortemousque P-A, Chanrion E, Thiney V, Ludwig A, Wieck AD, Urdampilleta M, Bäuerle C, Meunier T. Distant spin entanglement via fast and coherent electron shuttling. *Nat Nanotechnol*. 2021;16(5):570–5. <https://doi.org/10.1038/s41565-021-00846-y>.
70. Taubert D, Schinner GJ, Tranitz HP, Wegscheider W, Tomaras C, Kehrein S, Ludwig S. Electron-avalanche amplifier based on the electronic venturi effect. *Phys Rev B*. 2010;82:161416. <https://doi.org/10.1103/PhysRevB.82.161416>.
71. Taubert D, Tomaras C, Schinner GJ, Tranitz HP, Wegscheider W, Kehrein S, Ludwig S. Relaxation of hot electrons in a degenerate two-dimensional electron system: transition to one-dimensional scattering. *Phys Rev B*. 2011;83:235404. <https://doi.org/10.1103/PhysRevB.83.235404>.

72. Fletcher JD, See P, Howe H, Pepper M, Giblin SP, Griffiths JP, Jones GAC, Farrer I, Ritchie DA, Janssen TJBM, Kataoka M. Clock-controlled emission of single-electron wave packets in a solid-state circuit. *Phys Rev Lett*. 2013;111(21):216807. <https://doi.org/10.1103/PhysRevLett.111.216807>.
73. Emary C, Dyson A, Ryu S, Sim H-S, Kataoka M. Phonon emission and arrival times of electrons from a single-electron source. *Phys Rev B*. 2016;93(3):035436. <https://doi.org/10.1103/PhysRevB.93.035436>.
74. Emary C, Clark LA, Kataoka M, Johnson N. Energy relaxation in hot electron quantum optics via acoustic and optical phonon emission. *Phys Rev B*. 2019;99(4):045306. <https://doi.org/10.1103/PhysRevB.99.045306>.
75. Johnson N, Emary C, Ryu S, Sim H-S, See P, Fletcher JD, Griffiths JP, Jones GAC, Farrer I, Ritchie DA, Pepper M, Janssen TJBM, Kataoka M. LO-phonon emission rate of hot electrons from an on-demand single-electron source in a GaAs/AlGaAs heterostructure. *Phys Rev Lett*. 2018;121(13):137703. <https://doi.org/10.1103/PhysRevLett.121.137703>.
76. Ota T, Akiyama S, Hashisaka M, Muraki K, Fujisawa T. Spectroscopic study on hot-electron transport in a quantum Hall edge channel. *Phys Rev B*. 2019;99:085310. <https://doi.org/10.1103/PhysRevB.99.085310>.
77. Heiblum M, Nathan MI, Thomas DC, Knoedler CM. Direct observation of ballistic transport in gaas. *Phys Rev Lett*. 1985;55:2200–3. <https://doi.org/10.1103/PhysRevLett.55.2200>.
78. Akiyama S, Hirasawa T, Sato Y, Akiho T, Muraki K, Fujisawa T. Ballistic hot-electron transport in a quantum Hall edge channel defined by a double gate. *Appl Phys Lett*. 2019;115(24):243106. <https://doi.org/10.1063/1.5126776>.
79. Kataoka M, Johnson N, Emary C, See P, Griffiths JP, Jones GAC, Farrer I, Ritchie DA, Pepper M, Janssen TJBM. Time-of-flight measurements of single-electron wave packets in quantum Hall edge states. *Phys Rev Lett*. 2016;116(12):126803. <https://doi.org/10.1103/PhysRevLett.116.126803>.
80. Waldie J, See P, Kashcheyevs V, Griffiths JP, Farrer I, Jones GAC, Ritchie DA, Janssen TJBM, Kataoka M. Measurement and control of electron wave packets from a single-electron source. *Phys Rev B*. 2015;92(12):125305. <https://doi.org/10.1103/PhysRevB.92.125305>.
81. Kataoka M, Fletcher JD, Johnson N. Time-resolved single-electron wave-packet detection. *Phys Status Solidi B*. 2017;254(3):1600547. <https://doi.org/10.1002/pssb.201600547>.
82. Fletcher JD, Johnson N, Locane E, See P, Griffiths JP, Farrer I, Ritchie DA, Brouwer PW, Kashcheyevs V, Kataoka M. Continuous-variable tomography of solitary electrons. *Nat Commun*. 2019;10(5298):1–7. <https://doi.org/10.1038/s41467-019-13222-1>.
83. Locane E, Brouwer PW, Kashcheyevs V. Time-energy filtering of single electrons in ballistic waveguides. *New J Phys*. 2019;21:093042. <https://doi.org/10.1088/1367-2630/ab3fbb>.
84. Ryu S, Kataoka M, Sim H-S. Ultrafast emission and detection of a single-electron Gaussian wave packet: a theoretical study. *Phys Rev Lett*. 2016;117(14):146802. <https://doi.org/10.1103/PhysRevLett.117.146802>.
85. Ubbelohde N, Hohls F, Kashcheyevs V, Wagner T, Fricke L, Kästner B, Pierz K, Schumacher HW, Haug RJ. Partitioning of on-demand electron pairs. *Nat Nanotechnol*. 2015;10(1):46–9. <https://doi.org/10.1038/nnano.2014.275>.
86. Fricke L, Wulf M, Kaestner B, Kashcheyevs V, Timoshenko J, Nazarov P, Hohls F, Mirovsky P, Mackrodt B, Dolata R, Weimann T, Pierz K, Schumacher HW. Counting statistics for electron capture in a dynamic quantum dot. *Phys Rev Lett*. 2013;110:126803. <https://doi.org/10.1103/PhysRevLett.110.126803>.
87. Schulenburg J, Saptsov RB, Haupt F, Splettstoesser J, Wegewijs MR. Fermion-parity duality and energy relaxation in interacting open systems. *Phys Rev B*. 2016;93(8):081411. <https://doi.org/10.1103/PhysRevB.93.081411>.
88. Schulenburg J, Splettstoesser J, Wegewijs MR. Duality for open fermion systems: energy-dependent weak coupling and quantum master equations. *Phys Rev B*. 2018;98(23):235405. <https://doi.org/10.1103/PhysRevB.98.235405>.
89. Schulenburg J, Splettstoesser J, Governale M, Contreras-Pulido LD. Detection of the relaxation rates of an interacting quantum dot by a capacitively coupled sensor dot. *Phys Rev B*. 2014;89(19):195305. <https://doi.org/10.1103/PhysRevB.89.195305>.
90. Riwar R-P, Roche B, Jehl X, Splettstoesser J. Readout of relaxation rates by nonadiabatic pumping spectroscopy. *Phys Rev B*. 2016;93(23):235401. <https://doi.org/10.1103/PhysRevB.93.235401>.
91. Clark LA, Kataoka M, Emary C. Mitigating decoherence in hot electron interferometry. *New J Phys*. 2020;22(10):103031. <https://doi.org/10.1088/1367-2630/abb9e5>.
92. Barratt CJ, Ryu S, Clark LA, Sim H-S, Kataoka M, Emary C. Phase averaging and arrival times in a hot-electron Mach-Zehnder interferometer. 2021. [arXiv:2104.01653](https://arxiv.org/abs/2104.01653).
93. Haack G, Moskalets M, Splettstoesser J, Büttiker M. Coherence of single-electron sources from Mach-Zehnder interferometry. *Phys Rev B*. 2011;84(8):081303. <https://doi.org/10.1103/PhysRevB.84.081303>.
94. Juergens S, Splettstoesser J, Moskalets M. Single-particle interference versus two-particle collisions. *Europhys Lett*. 2011;96(3):37011. <https://doi.org/10.1209/0295-5075/96/37011>.
95. Splettstoesser J, Moskalets M, Büttiker M. Two-particle nonlocal Aharonov-Bohm effect from two single-particle emitters. *Phys Rev Lett*. 2009;103(7):076804. <https://doi.org/10.1103/PhysRevLett.103.076804>.
96. Johnson N, Fletcher JD, Humphreys DA, See P, Griffiths JP, Jones GAC, Farrer I, Ritchie DA, Pepper M, Janssen TJBM, Kataoka M. Ultrafast voltage sampling using single-electron wavepackets. *Appl Phys Lett*. 2017;110(10):102105. <https://doi.org/10.1063/1.4978388>.
97. Levitov LS, Lee H, Lesovik GB. Electron counting statistics and coherent states of electric current. *J Math Phys*. 1996;37(10):4845–66. <https://doi.org/10.1063/1.531672>.
98. Ivanov DA, Lee HW, Levitov LS. Coherent states of alternating current. *Phys Rev B*. 1997;56:6839–50. <https://doi.org/10.1103/PhysRevB.56.6839>.
99. Keeling J, Klich I, Levitov LS. Minimal excitation states of electrons in one-dimensional wires. *Phys Rev Lett*. 2006;97:116403. <https://doi.org/10.1103/PhysRevLett.97.116403>.
100. Grenier C, Dubois J, Jullien T, Rouleau P, Glatlil DC, Degiovanni P. Fractionalization of minimal excitations in integer quantum Hall edge channels. *Phys Rev B*. 2013;88:085302. <https://doi.org/10.1103/PhysRevB.88.085302>.
101. Moskalets M. First-order correlation function of a stream of single-electron wave packets. *Phys Rev B*. 2015;91:195431. <https://doi.org/10.1103/PhysRevB.91.195431>.
102. Glatlil DC, Rouleau P. Hanbury-Brown Twiss noise correlation with time controlled quasi-particles in ballistic quantum conductors. *Physica E, Low-Dimens Syst Nanostruct*. 2016;76:216–22. <https://doi.org/10.1016/j.physe.2015.10.034>.

103. Ferraro D, Ronetti F, Vannucci L, Acciai M, Rech J, Jockheere T, Martin T, Sassetti M. Hong-Ou-Mandel characterization of multiply charged Levitons. *Eur Phys J Spec Top.* 2018;227(12):1345–59. <https://doi.org/10.1140/epjst/e2018-800074-1>.
104. Vanević M, Gabelli J, Belzig W, Reulet B. Electron and electron-hole quasiparticle states in a driven quantum contact. *Phys Rev B.* 2016;93:041416. <https://doi.org/10.1103/PhysRevB.93.041416>.
105. Yin Y. Quasiparticle states of on-demand coherent electron sources. *J Phys Condens Matter.* 2019;31(24):245301. <https://doi.org/10.1088/1361-648x/ab0fc4>.
106. Kotilahti J, Burset P, Moskalets M, Flindt C. Multi-particle interference in an electronic Mach—Zehnder interferometer. *Entropy.* 2021;23(6):736. <https://doi.org/10.3390/e23060736>.
107. Grenier C, Hervé R, Bocquillon E, Parmentier FD, Plaças B, Berroir JM, Fève G, Degiovanni P. Single-electron quantum tomography in quantum Hall edge channels. *New J Phys.* 2011;13(9):093007. <https://doi.org/10.1088/1367-2630/13/9/093007>.
108. Roussel B, Cabart C, Fève G, Degiovanni P. Processing quantum signals carried by electrical currents. *PRX Quantum.* 2021;2:020314. <https://doi.org/10.1103/PRXQuantum.2.020314>.
109. Ferraro D, Feller A, Ghibaudo A, Thibierge E, Bocquillon E, Fève G, Grenier C, Degiovanni P. Wigner function approach to single electron coherence in quantum Hall edge channels. *Phys Rev B.* 2013;88:205303. <https://doi.org/10.1103/PhysRevB.88.205303>.
110. Ferraro D, Roussel B, Cabart C, Thibierge E, Fève G, Grenier C, Degiovanni P. Real-time decoherence of Landau and Levitov quasiparticles in quantum Hall edge channels. *Phys Rev Lett.* 2014;113:166403. <https://doi.org/10.1103/PhysRevLett.113.166403>.
111. Cabart C, Roussel B, Fève G, Degiovanni P. Taming electronic decoherence in one-dimensional chiral ballistic quantum conductors. *Phys Rev B.* 2018;98:155302. <https://doi.org/10.1103/PhysRevB.98.155302>.
112. Rebora G, Acciai M, Ferraro D, Sassetti M. Collisional interferometry of levitons in quantum Hall edge channels at $\nu = 2$. *Phys Rev B.* 2020;101:245310. <https://doi.org/10.1103/PhysRevB.101.245310>.
113. Wahl C, Rech J, Jonckheere T, Martin T. Interactions and charge fractionalization in an electronic Hong-Ou-Mandel interferometer. *Phys Rev Lett.* 2014;112:046802. <https://doi.org/10.1103/PhysRevLett.112.046802>.
114. Freulon V, Marguerite A, Berroir J-M, Plaças B, Cavanna A, Jin Y, Fève G. Hong-Ou-Mandel experiment for temporal investigation of single-electron fractionalization. *Nat Commun.* 2015;6:6854.
115. Marguerite A, Cabart C, Wahl C, Roussel B, Freulon V, Ferraro D, Grenier C, Berroir J-M, Plaças B, Jonckheere T, Rech J, Martin T, Degiovanni P, Cavanna A, Jin Y, Fève G. Decoherence and relaxation of a single electron in a one-dimensional conductor. *Phys Rev B.* 2016;94:115311. <https://doi.org/10.1103/PhysRevB.94.115311>.
116. Auston DH. Picosecond optoelectronic switching and gating in silicon. *Appl Phys Lett.* 1975;26(3):101–3. <https://doi.org/10.1063/1.88079>.
117. Mourou G, Stancampiano CV, Blumenthal D. Picosecond microwave pulse generation. *Appl Phys Lett.* 1981;38(6):470–2. <https://doi.org/10.1063/1.92407>.
118. Auston DH, Cheung KP, Smith PR. Picosecond photoconducting hertzian dipoles. *Appl Phys Lett.* 1984;45(3):284–6. <https://doi.org/10.1063/1.95174>.
119. Heshmat B, Pahlevaninezhad H, Pang Y, Masnadi-Shirazi M, Burton Lewis R, Tiedje T, Gordon R, Darcie TE. Nanoplasmonic terahertz photoconductive switch on GaAs. *Nano Lett.* 2012;12(12):6255–9. <https://doi.org/10.1021/nl303314a>.
120. Georgiou G, Geffroy C, Bäuerle C, Roux J-F. Efficient three-dimensional photonic—plasmonic photoconductive switches for picosecond THz pulses. *ACS Photonics.* 2020;7(6):1444–51. <https://doi.org/10.1021/acsp Photonics.0c00044>.
121. Roulleau P, Portier F, Glatli DC, Roche P, Cavanna A, Faini G, Gennser U, Mailly D. Finite bias visibility of the electronic Mach-Zehnder interferometer. *Phys Rev B.* 2007;76(16):161309. <https://doi.org/10.1103/PhysRevB.76.161309>.
122. Neder I, Ofek N, Chung Y, Heiblum M, Mahalu D, Umansky V. Interference between two indistinguishable electrons from independent sources. *Nature.* 2007;448:333.
123. Forrester DM, Kusmartsev FV. Graphene levitons and anti-levitons in magnetic fields. *Nanoscale.* 2014;6:7594–603. <https://doi.org/10.1039/C4NR00754A>.
124. Forrester DM. Confinement effects of levitons in a graphene cosmology laboratory. *RSC Adv.* 2015;5:5442–9. <https://doi.org/10.1039/C4RA11227J>.
125. Thalineau R, Wieck AD, Bäuerle C, Meunier T. Using a two-electron spin qubit to detect electrons flying above the Fermi sea. 2014. [arXiv:1403.7770](https://arxiv.org/abs/1403.7770).
126. Meunier T. private communication.
127. Glatli DC, Nath J, Taktak I, Roulleau P, Bäuerle C, Waintal X. Design of a single-shot electron detector with sub-electron sensitivity for electron flying qubit operation. 2020. <https://arxiv.org/abs/2002.03947>.
128. Ionićiu R, Amaratunga G, Udrea F. Quantum computation with ballistic electrons. *Int J Mod Phys B.* 2001;15(2):125–33.
129. Bertoni A, Bordone P, Brunetti R, Jacoboni C, Reggiani S. Quantum logic gates based on coherent electron transport in quantum wires. *Phys Rev Lett.* 2000;84:5912–5. <https://doi.org/10.1103/PhysRevLett.84.5912>.
130. Ionićiu R, Zanardi P, Rossi F. Testing Bell's inequality with ballistic electrons in semiconductors. *Phys Rev A.* 2001;63:050101. <https://doi.org/10.1103/PhysRevA.63.050101>.
131. Slussarenko S, Pryde GJ. Photonic quantum information processing: a concise review. *Appl Phys Rev.* 2019;6(4):041303. <https://doi.org/10.1063/1.5115814>.
132. Reiher M, Wiebe N, Svore KM, Wecker D, Troyer M. Elucidating reaction mechanisms on quantum computers. *Proc Natl Acad Sci USA.* 2017;114(29):7555–60. <https://doi.org/10.1073/pnas.1619152114>.
133. Zhou Y, Stoudenmire EM, Waintal X. What limits the simulation of quantum computers? *Phys Rev X.* 2020;10:041038. <https://doi.org/10.1103/PhysRevX.10.041038>.
134. Takeda S, Furusawa A. Universal quantum computing with measurement-induced continuous-variable gate sequence in a loop-based architecture. *Phys Rev Lett.* 2017;119:120504. <https://doi.org/10.1103/PhysRevLett.119.120504>.
135. Waintal X. What determines the ultimate precision of a quantum computer. *Phys Rev A.* 2019;99:042318. <https://doi.org/10.1103/PhysRevA.99.042318>.

136. Glattli DC, Andrei EY, Deville G, Poitrenaud J, Williams FIB. Dynamical Hall effect in a two-dimensional classical plasma. *Phys Rev Lett*. 1985;54:1710–3. <https://doi.org/10.1103/PhysRevLett.54.1710>.
137. Mast DB, Dahm AJ, Fetter AL. Observation of bulk and edge magnetoplasmons in a two-dimensional electron fluid. *Phys Rev Lett*. 1985;54:1706–9. <https://doi.org/10.1103/PhysRevLett.54.1706>.
138. Dahm AJ, Vinen WF. Electrons and ions at the helium surface. *Phys Today*. 1987;40(2):43–50. <https://doi.org/10.1063/1.881098>.
139. Byeon H, Nasyedkin K, Lane JR, Beysengulov NR, Zhang L, Loloee R, Pollanen J. Piezoacoustics for precision control of electrons floating on helium. *Nat Commun*. 2021;12(1):4150. <https://doi.org/10.1038/s41467-021-24452-7>.
140. Zhou X, Koolstra G, Zhang X, Yang G, Han X, Dizdar B, Li X, Divan R, Guo W, Murch KW, Schuster DI, Jin D. Single electrons on solid neon as a solid-state qubit platform. *Nature*. 2022;605(7908):46–50. <https://doi.org/10.1038/s41586-022-04539-x>.
141. Chatterjee A, Stevenson P, De Franceschi S, Morello A, de Leon NP, Kuemmeth F. Semiconductor qubits in practice. *Nat Rev Phys*. 2021;3(3):157–77. <https://doi.org/10.1038/s42254-021-00283-9>.
142. Trellakis A, Zibold T, Andlauer T, Birner S, Smith RK, Morschl R, Vogl P. The 3D nanometer device project nextnano: concepts, methods, results. *J Comput Electron*. 2006;5(4):285–9. <https://doi.org/10.1007/s10825-006-0005-x>.
143. Groth CW, Wimmer M, Akhmerov AR, Waintal X. Kwant: a software package for quantum transport. *New J Phys*. 2014;16(6):063065. <https://doi.org/10.1088/1367-2630/16/6/063065>.
144. Kloss T, Weston J, Gaury B, Rossignol B, Groth C, Waintal X. Tkwant: a software package for time-dependent quantum transport. *New J Phys*. 2021;23(2):023025. <https://doi.org/10.1088/1367-2630/abddf7>.
145. Bautze T, Süssmeier C, Takada S, Groth C, Meunier T, Yamamoto M, Tarucha S, Waintal X, Bäuerle C. Theoretical, numerical, and experimental study of a flying qubit electronic interferometer. *Phys Rev B*. 2014;89:125432. <https://doi.org/10.1103/PhysRevB.89.125432>.
146. Weston J, Waintal X. Towards realistic time-resolved simulations of quantum devices. *J Comput Electron*. 2016;15(4):1148–57. <https://doi.org/10.1007/s10825-016-0855-9>.
147. Rossignol B, Kloss T, Armagnat P, Waintal X. Toward flying qubit spectroscopy. *Phys Rev B*. 2018;98:205302. <https://doi.org/10.1103/PhysRevB.98.205302>.
148. Datta S. Quantum transport: atom to transistor. Cambridge: Cambridge University Press; 2005. <https://doi.org/10.1017/CBO9781139164313>.
149. Birner S, Schindler C, Greck P, Sabathil M, Vogl P. Ballistic quantum transport using the contact block reduction (CBR) method. *J Comput Electron*. 2009;8:267–86. <https://doi.org/10.1007/s10825-009-0293-z>.
150. Trellakis A, Galick AT, Pacelli A, Ravaoli U. Iteration scheme for the solution of the two-dimensional Schrödinger-Poisson equations in quantum structures. *J Appl Phys*. 1997;81(12):7880–4. <https://doi.org/10.1063/1.365396>.
151. Armagnat P, Lacerda-Santos A, Rossignol B, Groth C, Waintal X. The self-consistent quantum-electrostatic problem in strongly non-linear regime. *SciPost Phys*. 2019;7:31. <https://doi.org/10.21468/SciPostPhys.7.3.031>.
152. Grange T, Stark D, Scalari G, Faist J, Persichetti L, Di Gaspare L, De Seta M, Ortolani M, Paul DJ, Capellini G, Birner S, Virgilio M. Room temperature operation of n-type Ge/SiGe terahertz quantum cascade lasers predicted by non-equilibrium Green's functions. *Appl Phys Lett*. 2019;114(11):111102. <https://doi.org/10.1063/1.5082172>.
153. Mamaluy D, Sabathil M, Vogl P. Efficient method for the calculation of ballistic quantum transport. *J Appl Phys*. 2003;93:4628. <https://doi.org/10.1063/1.1560567>.
154. Birner S, Hackenbuchner S, Sabathil M, Zandler G, Majewski J, Andlauer T, Zibold T, Morschl R, Trellakis A, Vogl P. Modeling of semiconductor nanostructures with nextnano³. *Acta Phys Pol A*. 2006;110:111–24. <https://doi.org/10.12693/APhysPolA.110.111>.
155. Birner S, Zibold T, Andlauer T, Kubis T, Sabathil M, Trellakis A, Vogl P. nextnano: general purpose 3-D simulations. *IEEE Trans Electron Devices*. 2007;54:2137–42. <https://doi.org/10.1109/TED.2007.902871>.
156. Zibold T, Vogl P, Bertoni A. Theory of semiconductor quantum-wire-based single- and two-qubit gates. *Phys Rev B*. 2007;76:195301. <https://doi.org/10.1103/PhysRevB.76.195301>.
157. Caflisch RE, Gyure MF, Robinson HD, Yablonovitch E. Modeling, design, and optimization of a solid state electron spin qubit. *SIAM J Appl Math*. 2005;65(4):1285–304.
158. Wild A, Sailer J, Nützel J, Abstreiter G, Ludwig S, Bougeard D. Electrostatically defined quantum dots in a Si/SiGe heterostructure. *New J Phys*. 2010;12(11):113019. <https://doi.org/10.1088/1367-2630/12/11/113019>.
159. Ramirez EB, Sfakakis F, Kudva S, Baugh J. Few-electrode design for silicon MOS quantum dots. *Semicond Sci Technol*. 2019;35(1):015002. <https://doi.org/10.1088/1361-6641/ab516a>.
160. Buonacorsi B, Shaw B, Baugh J. Simulated coherent electron shuttling in silicon quantum dots. *Phys Rev B*. 2020;102:125406. <https://doi.org/10.1103/PhysRevB.102.125406>.
161. Jirovec D, Hofmann A, Ballabio A, Mutter PM, Tavani G, Botifoll M, Crippa A, Kukucka J, Sagi O, Martins F et al. A singlet-triplet hole spin qubit in planar ge. *Nat Mater*. 2021;20:1106–12.
162. Chatzikyriakou E, Wang J, Mazzella L, Lacerda-Santos A, Figueira MCdS, Trellakis A, Birner S, Grange T, Bäuerle C, Waintal X. Unveiling the charge distribution of a GaAs-based nanoelectronic device: a large experimental data-set approach. 2022. <https://arxiv.org/abs/2205.00846>.
163. Hou H, Chung Y, Rughoobur G, Hsiao TK, Nasir A, Flewitt AJ, Griffiths JP, Farrer I, Ritchie DA, Ford CJB. Experimental verification of electrostatic boundary conditions in gate-patterned quantum devices. *J Phys D, Appl Phys*. 2018;51(24):244004.
164. Wang J. nextnanopy. 2021. <https://github.com/nextnanopy> Accessed 2021-08-03.
165. Datta S, Melloch MR, Bandyopadhyay S, Lundstrom MS. Proposed structure for large quantum interference effects. *Appl Phys Lett*. 1986;48(7):487–9. <https://doi.org/10.1063/1.96484>.
166. Gaury B, Weston J, Santin M, Houzet M, Groth C, Waintal X. Numerical simulations of time-resolved quantum electronics. *Phys Rep*. 2014;534(1):1–37. <https://doi.org/10.1016/j.physrep.2013.09.001>.
167. Gaury B, Weston J, Waintal X. Stopping electrons with radio-frequency pulses in the quantum Hall regime. *Phys Rev B*. 2014;90:161305. <https://doi.org/10.1103/PhysRevB.90.161305>.
168. Maček M, Dumitrescu PT, Bertrand C, Triggs B, Parcollet O, Waintal X. Quantum quasi-Monte Carlo technique for many-body perturbative expansions. *Phys Rev Lett*. 2020;125:047702. <https://doi.org/10.1103/PhysRevLett.125.047702>.

169. Lepeshov S, Gorodetsky A, Krasnok A, Rafailov E, Belov P. Enhancement of terahertz photoconductive antenna operation by optical nanoantennas. *Laser Photonics Rev.* 2017;11(1):1600199.
<https://doi.org/10.1002/lpor.201600199>.
170. Bashirpour M, Ghorbani S, Kolahdouz M, Neshat M, Masnadi-Shirazi M, Aghababa H. Significant performance improvement of a terahertz photoconductive antenna using a hybrid structure. *RSC Adv.* 2017;7:53010–7.
<https://doi.org/10.1039/C7RA11398F>.

Submit your manuscript to a SpringerOpen[®] journal and benefit from:

- Convenient online submission
- Rigorous peer review
- Open access: articles freely available online
- High visibility within the field
- Retaining the copyright to your article

Submit your next manuscript at ► [springeropen.com](https://www.springeropen.com)